
Princeton Plasma Physics Laboratory

PPPL-5223

A Review of NSTX Research 1999-2015

S. M. Kaye

August 2015



Prepared for the U.S. Department of Energy under Contract DE-AC02-09CH11466.

Princeton Plasma Physics Laboratory

Report Disclaimers

Full Legal Disclaimer

This report was prepared as an account of work sponsored by an agency of the United States Government. Neither the United States Government nor any agency thereof, nor any of their employees, nor any of their contractors, subcontractors or their employees, makes any warranty, express or implied, or assumes any legal liability or responsibility for the accuracy, completeness, or any third party's use or the results of such use of any information, apparatus, product, or process disclosed, or represents that its use would not infringe privately owned rights. Reference herein to any specific commercial product, process, or service by trade name, trademark, manufacturer, or otherwise, does not necessarily constitute or imply its endorsement, recommendation, or favoring by the United States Government or any agency thereof or its contractors or subcontractors. The views and opinions of authors expressed herein do not necessarily state or reflect those of the United States Government or any agency thereof.

Trademark Disclaimer

Reference herein to any specific commercial product, process, or service by trade name, trademark, manufacturer, or otherwise, does not necessarily constitute or imply its endorsement, recommendation, or favoring by the United States Government or any agency thereof or its contractors or subcontractors.

PPPL Report Availability

Princeton Plasma Physics Laboratory:

<http://www.pppl.gov/techreports.cfm>

Office of Scientific and Technical Information (OSTI):

<http://www.osti.gov/scitech/>

Related Links:

[U.S. Department of Energy](#)

[U.S. Department of Energy Office of Science](#)

[U.S. Department of Energy Office of Fusion Energy Sciences](#)

A Review of NSTX Research 1999-2015
(the unabridged version)

Contribution to appear as a chapter in:
**Magnetic Fusion Energy: From Experiments to
Power Plants**, edited by G. H. Neilson

S. M. Kaye
Princeton Plasma Physics Laboratory
Princeton University
Princeton, NJ 08543 USA

I. Introduction

The National Spherical Torus eXperiment (NSTX) was a medium-sized Spherical Tokamak (ST) whose aim is to:

1. Establish attractive ST operating scenarios and configurations
2. Complement tokamak physics and support ITER
3. Understand the unique physics properties of the ST.

The goal of the first mission element is to utilize advantages of the ST configuration for addressing key gaps between ITER performance and the expected performance of an ST-based FNSF¹ or ST-based DEMO². One such gap is fully non-inductive operation. To achieve the second mission element, NSTX would exploit unique ST features to improve tokamak understanding, such as by leveraging the unique ST parameter range to benchmark and validate theories that could then be used to predict performance in future devices. Furthermore, NSTX would contribute to ITER final design activities and research preparation. The unique ST properties consist of large toroidicity, very high β_T , high $v_{fast}/v_{Alfvén}$ and high ExB shearing rate.

In order to accomplish its mission, NSTX was designed, constructed and operated at the Princeton Plasma Physics Laboratory, Princeton University, Princeton NJ, USA with the following capabilities^{3,4}:

1. $R/a = 0.85/0.68 \text{ m} \sim 1.26$
2. 0.6 Weber of ohmic solenoidal flux for inductive plasma current initiation, rampup and sustainment. Initiation is aided by 30 kW of 19 GHz electron cyclotron heating.
3. I_p up to 1.5 MA, B_T up to 0.55 T
4. D^+ or He^{++} plasma operation

5. Plasma elongations κ up to 2.5 and triangularities δ up to 0.8
6. Operation with deuterium (most of discharges) or helium plasmas.
7. Ability to operate in double-null (DN), lower single null (LSN) or upper single null (USN) divertor configurations. More recent configurational development included operation with a “snowflake” divertor⁵.
8. Auxiliary heating powers up to 7.2 MW of D⁰ neutral beam injection (W_{beam} up to 100 keV and tangency radii of $R_{\text{TAN}} \sim 50, 60$ and 70 cm for the three beam sources), and up to 6 MW of High Harmonic Fast Wave (HHFW) heating and current drive. The auxiliary heating and maximum current capabilities allow for plasma operation at low collisionality.
9. Co-axial Helicity Injection (CHI) for non-inductive plasma initiation^{6,7}.
10. A close-fitting conducting shell for passive stabilization of external MHD modes such as kinks and Resistive Wall Modes (RWMs), and active control of error fields and MHD modes through application of $n=1$ to 3 edge magnetic perturbations by a set of ex-vessel midplane coils. These capabilities allow for longer pulse lengths (up to 1.6 s) and achievement of higher $\beta_{\text{T}}, \beta_{\text{N}}$ by stabilizing MHD modes and delaying disruptions.
11. Different wall conditioning options, including:
 - a. Boronization and between-shots Helium Glow Discharge Cleaning (HeGDC + boronization)
 - b. Pre-discharge injection of lithium wall coatings by two downward-pointing LITHium EvaporatoRs (LITERS)⁸

Lithium as a Plasma Facing Component (PFC) was also investigated with four heated Liquid Lithium Divertor (LLD) modules⁹. A schematic and photo of the LITERS and LLD respectively can be seen in Fig. 1.

A full schematic of the NSTX vessel and an interior view is shown in Fig. 2. The vessel has electrical insulation between the center-stack and outer vacuum vessel (the “CHI gap”) to allow for a 2 kV DC bias voltage for CHI. Poloidal field (PF) coils are used for plasma shaping, and the mid-plane ex-vessel Error Field/Resistive Wall Mode, or Magnetic Perturbation (MP), coils allow for application of $n=1$ to 3 edge magnetic perturbations. The close-fitting shell is made out of copper, with graphite tiles for Plasma Facing Components. The close-fitting shell, as well as lithium wall conditioning, HHFW and CHI capabilities are among the features that distinguish NSTX from the complementary MAST device, which will be described in the next Chapter.

NSTX has a complete set of diagnostics to measure plasma performance, including, but not limited to, electron temperature and density profiles from Thomson Scattering, ion temperature, rotation and impurity density profiles from Charge-Exchange Recombination Spectroscopy (CHERS), magnetic field pitch (B_p/B_T , where the subscripts ‘p’ ‘T’ indicate poloidal and toroidal direction respectively) from Motional Stark Effect (MSE) spectroscopy, midplane bolometer arrays, various spectroscopic diagnostics both in the divertor and main chamber for impurity content, magnetics (flux loops, Mirnov coils) with excellent spatial coverage and with the ability to measure magnetic fluctuations from DC up to the ion cyclotron frequency (\sim MHz), high- k scattering and Beam Emission Spectroscopy (BES) for measuring electron-scale and ion-scale turbulence respectively, multi-energy soft X-ray arrays for electron temperature and MHD mode measurements, Gas Puff Imaging (GPI) for measuring edge turbulence, edge reflectometers, Langmuir probes in the divertor, visible and IR cameras (the latter for measuring heat loads on the PFCs) and D_α arrays.

NSTX began physics operation in Feb. 1999, and operated for over a decade, until ceasing operations in Oct. 2010 to allow for an enhancement and upgrade of the device and auxiliary heating capabilities. During the first year of operation, NSTX achieved plasma currents of up to 1 MA with optimized ohmic flux consumption,

found ohmic confinement times increasing with density up to values of $\tau_E/\tau_{89p} \sim 1$ at $n_e/n_{GW} \sim 0.7$ ($\langle v_e^* \rangle \sim 1$) and then saturating at higher density, observed predominant $n=1$ activity that led to sawteeth, reconnection events or disruptions, and tested CHI, HHFW and NB capabilities⁴. Even with low injected neutral beam power (~ 2.8 MW), β_T values of up to 18% were obtained.

With the introduction of higher levels of auxiliary heating power as well as enhanced operational capabilities over the next two years, NSTX made rapid progress towards achieving its goal of high β_T , long-pulse performance¹⁰. Results included:

- β_T values up to 35%, with β_N up to 6.5 m-T-MA⁻¹ and β_N/l_i up to 10
- Pulse lengths up to 1 s with 60 to 65% of the current being driven non-inductively by both bootstrap and neutral beam current drive
- H-mode operation with $\tau_E/\tau_{98y,2}$ values up to 1.5 and τ_E/τ_{89p} values over 2
- Impurity transport rates near predicted neoclassical values in turbulent L-mode plasmas
- Signatures of neoclassical tearing modes and resistive wall modes
- Several classes of fast ion-induced MHD, with modes in the conventional Alfvén Eigenmode (AE) range of frequencies (tens of kHz), but also AEs with frequencies of 0.5-1 MHz, which is near the ion cyclotron frequency
- Significant electron heating and indications of current drive with HHFW
- Noninductive startup currents of up to 400 kA using CHI
- Initial edge heat flux studies in quiescent H-modes

In the following sections, topical summaries of NSTX results, with emphasis on those from the latter half of the NSTX operational lifetime. Summaries of NSTX results

over successive two year periods can be found in IAEA Overview papers^{4,10,11,12,13,14,15,16} as well as in a recently published ST review paper¹⁷. In the last section, the mission elements and operational capabilities of the NSTX-Upgrade device¹⁸, or NSTX-U, will be described. NSTX-U is scheduled to commence physics operation in mid-2015.

II. Transport and Turbulence

Prior to NSTX being put into operation, studies indicated the potential for reduced anomalous ion transport at low aspect ratio due to the strong toroidicity¹⁹ and large ExB shearing rate^{3,10}. The first characteristic means that a field line will encounter the good curvature region, where the drive for ion-scale microturbulence is reduced, over an extended measure of its length, and the second feature means that any residual turbulence can be reduced by rapid shearing of turbulent eddies. Consequently, ion transport was predicted, at least for some cases, to be at the neoclassical level. Little was studied for electron turbulence at low aspect ratio prior to NSTX operation, although it was recognized that the high- β nature of NSTX, and thus electromagnetic effects, could potentially impact both electron and ion transport.

With good wall conditioning, access to the H-mode in NSTX required only a few hundred kW²⁰, and the H-mode could be obtained easily in ohmic plasmas. H-mode access was optimized using in-board fueling, and L-H thresholds in helium plasmas were 20 to 40% greater than those in deuterium. Applied 3D magnetic fields increased the L-H threshold, possibly due to decrease in rotation and associated ExB shear. Plasmas with lithium wall conditioning exhibited threshold powers approximately 50% less than boronized plasmas²¹, and unlike at conventional aspect ratio, the L-H threshold power depended linearly on plasma current^{22,21}. It was determined from XGC0²³ calculations that this current dependence was due to differences in the E_r well depth as determined by neoclassical processes²¹. The threshold was also lower in lower triangularity discharges where the separatrix X-point was at larger major radius. This latter result was also consistent with

expectations from neoclassical transport and orbit loss, as determined by XGC0 calculations²⁴.

The L-mode global confinement scaling showed similar parametric dependences as scalings found by conventional aspect ratio devices²⁵, although with a stronger B_T and weaker P_{loss} dependence, with $\tau_E \sim I_p^{1.01} B_T^{0.70} n_e^{0.07} P_{\text{loss}}^{-0.37}$. On the other hand, H-mode scalings were found to be more complicated. For discharges using HeGDC + boronization for wall conditioning, the thermal confinement scalings exhibited a strong, nearly linear dependence on B_T , and a weaker dependence on I_p ($\sim I_p^{0.35}$)^{26,27}. This is shown in the top panel of Fig. 3. This is in contrast to the scalings found at conventional aspect ratio, which went as $I_p^{0.9} B_T^{0.3}$, as captured in the ITER98y,2 scaling²⁸. In lithium conditioned NSTX plasmas, however, the parametric dependences were found to be similar to those of the ITER98y,2 scaling (Fig. 3, bottom panel). The two disparate results were reconciled by considering the dependence of confinement time on more fundamental physics variables. Fig. 4 shows that, for constrained ranges of β and ρ^* , the normalized confinement time ($\sim \Omega \tau_E \sim B \tau_E$) is a strong function of collisionality, increasing with decreasing ν^* in almost an inversely linear fashion²⁹. Shown in the figure are results from a collection of plasmas using the two different wall conditioning techniques. The primary reason for the improvement of confinement is a continual broadening of the electron temperature profile and associated reduction in electron transport as collisionality is reduced.

While global confinement studies can give an overview of the overall performance trends in plasmas, only detailed studies of local electron and ion transport, coupled with turbulence measurements and non-linear gyrokinetic code calculations, can truly reveal the processes controlling confinement in NSTX.

In H-mode discharges, the ion transport was near neoclassical levels, while the electron transport was dominant and highly anomalous, as shown in Fig. 5. There was, however, no single process underlying electron transport in different operational regimes or even with location within the plasma core. This is seen in Fig.

6, which shows the importance and scaling of various modes with collisionality and electron β . Shown in the figure are microtearing (MT), kinetic ballooning (KBM), electron temperature gradient (ETG) and ion temperature gradient/trapped electron modes (ITG/TEM). The results shown are taken from linear GYRO calculations, and they show a strong scaling of microtearing with both β and collisionality, while ETG shows little dependence on the latter. The ITG/TEM and ETG occur at low β , while the KBM exists at high β and low collisionality.

Microtearing modes, small-scale tearing modes with large toroidal mode numbers, but which are on the ion-gyroradius scale in poloidal extent ($k_r \rho_s < 1$), are driven unstable by electron temperature profile gradients at relatively high collisionality and finite β . Electron transport is driven by tearing-mode induced island overlap. The potential importance of microtearing in NSTX was recognized in linear gyrokinetic calculations^{30,31}, and recent non-linear gyrokinetic calculations using the GYRO code³² showed good agreement between experimentally inferred and calculated gyroBohm-normalized electron thermal diffusivities in the mid-region of the plasma due to microtearing, as seen in Fig. 7^{33,34}. In addition, the calculated diffusivity exhibited a dependence on collisionality consistent with the confinement improvement trend observed in Fig. 4, with microtearing being stabilized as collisionality decreased. It was shown that a microtearing-based reduced electron transport model could successfully predict T_e profiles for NSTX plasmas in which microtearing modes were calculated to be unstable.³⁵ As collisionality decreased, however, the Kinetic Ballooning Mode (KBM) is calculated to be more and more unstable.

At low β and with large electron temperatures and temperature profile gradients due to HHFW heating, electron transport was found to be controlled by Electron Temperature Gradient (ETG) modes, which occur on electron-gyroradius scales ($k_r \rho_s \sim 10-30$) and which are measured by the unique microwave scattering diagnostic on NSTX (Fig. 8). It was found the ETG turbulence increased when the electron temperature gradient exceeded the predicted ETG critical gradient^{36,37}, and

non-linear gyrokinetic simulations using the global code GTS³⁸ showed electron thermal diffusivities due to ETG quantitatively agreeing with those inferred from experiment^{39,40}. The ETG was further found to be stabilized by reversed magnetic shear, allowing for electron temperature gradients much greater than the critical gradient^{41,42}, and it was stabilized also by steep density gradients in the plasma edge, such as occurs after an ELM event⁴³.

The last primary cause of electron transport was hypothesized to be caused by high-frequency ($\sim\omega_{ci}$) Compressional and Global Alfvén Eigenmodes (CAE/GAEs), which occur in the central region of the plasma. An increase in CAE/GAE mode amplitude was correlated with increased NB heating power, with core electron temperatures that remained nearly constant, but broader T_e profiles, even with a tripling of the beam power^{44,45}. Assuming classical NB deposition profiles, electron thermal diffusivity values in the center of the plasma of up to 50 m²/s could be reached in the presence of CAE/GAEs, not inconsistent with theoretical estimates based on bursting CAE/GAE activity⁴⁵. Recent work, however, has suggested that the assumption of classical NB deposition may be wrong, as it has suggested that CAEs in the central plasma region can couple to Kinetic Alfvén Waves (KAW) farther out from the center, effectively producing a channeling of beam energy from the central region to farther out, to the KAW location⁴⁶. This will broaden the beam deposition profile, and is consistent with a broadening of the T_e profile outside the center and unchanged T_e in the center with increasing beam power and CAE activity. Rough estimates indicate a power flow of approximately 500 kW, which could affect the T_e by up to 0.5 keV.

As mentioned previously, prior to NSTX operations, theory calculations led to the expectation that ion transport could be at the neoclassical level under certain circumstances¹⁹. It was found that with NB heating, the ion transport was indeed at the neoclassical level over most of the plasma profile in H-mode plasmas at relatively high collisionality^{26,27}. However, as collisionality decreased and electron transport decreased with it, ion transport was found to actually increase to

anomalous levels with decreasing collisionality (Fig. 9). It is believed that this may be due to the increasing importance of the KBM or other ion-scale microturbulence at lower collisionality.

Momentum transport on NSTX was studied in both steady-state and using a combination of neutral beam pulses and pulses of $n=3$ magnetic fields applied to the plasma by the external MP coils. Steady-state momentum balance in H-mode plasmas showed effective momentum diffusivities (which include conduction and convection information), well in excess of those predicted by neoclassical theory (which were nearly zero), while the ion energy diffusivity in these plasmas was near neoclassical (much greater than zero for the ion energy transport)⁴⁷. Thus, the momentum transport could reflect residual ion scale turbulence that cannot be discerned from the ion energy transport owing to the large neoclassical component. In the perturbative experiments, the diffusive and convective (pinch) terms could be separated, and radially inward momentum pinches of up to 40 m/s in the outer region of the plasma were inferred^{48,47}. This led to a factor of a 50% effect between the effective and true momentum diffusivity (with the true diffusivity increased relative to the effective diffusivity). Low- k turbulence theories^{49,50} do predict values for the inward momentum pinch that are consistent with those inferred from experiment.

Main species and electron particle transport studies were problematic in NSTX owing to the complexity of modeling particle sources, lack of knowledge of the neutral density profiles, the relevant atomic physics and the interaction among the plasma and impurity species. Impurity transport, however, was investigated using controlled impurity gas injection. Early experiments using neon puffs and measurements by soft X-ray arrays, coupled to impurity transport calculations using the MIST⁵¹ and STRAHL⁵² codes, showed impurity diffusivities and radial velocities consistent with neoclassical predictions for both L- and H-mode in the plasma core ($r/a < 0.8$)^{53,54}. More recent studies of carbon and lithium transport indicated that while the lithium and core carbon profiles as well were consistent with those

predicted by neoclassical transport theory, anomalous transport was needed to reproduce the carbon density profile and its evolution in the pedestal region ($r/a > 0.8$)⁵⁵.

II. Macroscopic Stability

Because of operation at low toroidal field, STs naturally operate at high- β_T and β_N , especially with significant amounts of auxiliary heating power. High β_T optimizes both fusion reactivity and device cost, and high β_N operations optimizes the non-inductive bootstrap fraction, with $f_{bs} \sim A^{-0.5}(1+\kappa^2)\beta_N^2/\beta_T$. Thus, it is important for STs to produce stable plasmas at both high β_N (β_T) and high κ , the latter parameter being readily controllable. STs are generally designed for high κ (≥ 2.5). Understanding the macroscopic stability of NSTX plasmas both below and above the no-wall limit necessitated the use of linear and non-linear ideal and resistive MHD stability calculations. Error fields, neoclassical tearing modes, resistive wall modes and disruptions all inhibit achievement of high- β , and these will be discussed in this section, as will the effects of neoclassical toroidal viscosity produced by the application of 3D edge magnetic perturbations.

The highest β_T achieved on NSTX was approximately 40%, and this occurred in a discharge whose evolution is shown in Fig. 10¹¹. The β_T value is corroborated by EFIT equilibrium reconstructions^{56,57} and by TRANSP^{58,59} calculations. This high- β_T value corresponds to $\beta_N=6$. This discharge ended in a disruption (not shown in figure). The overall MHD stability database¹⁵ is shown in Fig. 11, where β_N is plotted as a function of l_i . Several results are noteworthy. β_N values up to 7, with β_N/l_i up to 14, were achieved. Discharges with $n=1$ active resistive wall mode (RWM) control (red points) achieve slightly higher β_N , β_N/l_i and lower l_i than those without active control (cyan points). Blue points are long pulse, ≥ 1 sec, plasmas, which are produced using active RWM control. This discharge duration corresponded to current flat-top times up to 40 to 50 times the energy confinement time and up to three to five times the current redistribution time. The database of points indicate a

large number of discharges that exceeded the $n=1$ no-wall limit ($\beta_N/l_i \sim 6.7$), which is not surprising given both the passive and active stabilization capabilities of NSTX. It is also seen that the β_N , β_N/l_i and l_i values are within the range expected for both an ST-FNSF and an ST Pilot Plant.

Error fields (EF) naturally occur in tokamaks due to static coil asymmetries as well as dynamic changes in the TF coil with respect to other coils, that are primarily the result of $\text{OH} \times \text{TF}$ forces. Rotation can shield the plasma from EF effects, unless the EF is so large, especially at low density, that it leads to a large island that can lock and result in a disruption. It is critical to determine the EF threshold for locking as function of density in order to be able to reduce the field below the threshold value through static and dynamic EF control. The Ideal Perturbed Equilibrium Code (IPEC)⁶⁰, which calculates the shielding currents, ideal plasma response and the resonant field at the m/n surface has been used to show that including the plasma response is crucial for determining the locking threshold. Fig. 12 shows the δB_{21} of the vacuum field and the total field, the latter as calculated by IPEC, as a function of density. Without plasma response, the locking threshold appears to saturate, but the plasma response tends to amplify the resonant $2/1$ EF, and the IPEC results recapture the linear scaling of locking threshold with density, even at high β_T (high n_e). With this knowledge, the midplane MP coils were used to offset and minimize the effect of the $2/1$ island by balancing the resonant $m=2$ and $m=0$ components of the EF¹². Closed loop feedback for dynamic correction of the $\text{OH} \times \text{TF}$ EF was also employed, resulting in a doubling of the duration that the plasma remained above the no-wall limit.

Neoclassical tearing modes (NTMs), islands destabilized by the helical perturbation resulting from the bootstrap current in the island itself, tend to be more stable in STs than in devices at conventional aspect ratio. This may be due to the stronger shaping, high- β and high- q operation, which are stabilizing. The difference in NTM stability as a function of aspect ratio was studied by determining the marginal island width for unstable growth of the NTM in NSTX and DIII-D⁶¹. The results of this

comparison showed the advantage of the ST, with the marginal island width scaling as $\varepsilon^{1/2}\rho_{oi}$ at the m/n rational surfaces. Here ε is inverse aspect ratio and ρ_{oi} is the poloidal ion gyroradius. The results showed that the magnetic curvature term, which is stabilizing, is more important in NSTX than in DIII-D, consistent with the decreased susceptibility to NTMs.

The close-fitting outboard passive conducting shell in NSTX slowed the growth rate of the ideal kink mode to the much slower timescale of the resistive wall mode (RWM), which, with passive and active stabilization, allowed the plasma to exceed the no-wall β -limit and approach the ideal (with wall) limit. This was the case primarily due to the strong outward ballooning character of the RWM, as determined from visible light camera images, electron temperature measurements and resistive DCON calculations^{62,63}. Active RWM control was accomplished through a feedback control loop using the MP coils to provide the offset to the detected mode amplitude and structure. Active control results in significant extensions in pulse length of high- β plasmas (Fig. 13). Also, an RWM state-space controller, incorporating $n=1$ RWM mode eigenfunctions, was used to enhance stabilization¹⁵.

As the plasma β evolved beyond the no-wall limit, the RWM amplitude grew, and early work suggested that rotation alone could stabilize the mode⁶⁴. However, on NSTX it was found that the RWM in some high rotation discharges could be even more unstable than in lower rotating plasmas⁶⁵. Including kinetic effects in the stability analysis, however, led to a more complete understanding of RWM stabilization physics^{66,67}. Enhanced stabilization of the RWM occurs when the plasma rotation is resonant with one of the characteristic kinetic frequencies, such as the precession drift or bounce frequencies. RWMs are more unstable if the plasma rotation falls between these resonances. MISK⁶⁸ calculations were used to show that on resonance, decreased collisionality is predicted to increase stabilization, while no collisionality dependence is predicted for off-resonance⁶⁹. These predictions were confirmed by measuring the resonant field amplification (RFA) by $n=1$ MHD spectroscopy⁶⁷. Fig. 14a shows the RFA plotted as a function of

ExB rotation frequency ($\langle\omega_E\rangle$), and there is clearly an optimal rotation profile for stable operation (minimum RFA). At that value of $\langle\omega_E\rangle$, the plasma is on-resonance with the precession drift frequency. Fig. 14b shows that on resonance the RFA decreases with decreasing collisionality (RWM more stable), while there is no change in RFA with collisionality off resonance, consistent with theory.

In plasmas with stable RWM, an Ideal Wall Mode (IWM) can be driven unstable near the ideal wall limit. The IWM has much higher frequencies and growth rates than the RWM. Recent MARS-K linear calculations have shown that, similar to the RWM, both rotation and kinetic effects can modify IWM stability limits. At low- β ($\beta_N < 3.5$), the kinetic effects are minimal, with the kinetic stability limit similar to the fluid limit. At higher β , however, the calculated and observed stability limits agree only when both effects are taken into account in a self-consistent fashion⁷⁰.

In principle, the rotation profile near the plasma edge can be controlled by application of 3D MPs, which produce a drag on the plasma. There have been several recent efforts that have extended the initial work on neoclassical toroidal viscosity (NTV)⁷¹. In one approach, the POCA (Particle Orbit Code for Anisotropic Pressure) code was developed to follow guiding center orbits for precisely calculating the perturbed particle distribution function in a non-axisymmetric ideal MHD equilibrium determined by IPEC⁷². POCA simulations show the importance of collisionality and particle resonances with toroidal rotation, similar to that found for RWMs. Another approach uses the Shaing formulation of NTV⁷³, which is valid in all collisionality regimes, and it computes δB fields in 3D as implemented in the NTVTOK code⁷⁴. This latter analysis has shown the importance of averaging the numerical results over the ion banana width to order to compare to experimental results. Comparisons of the numerical results from both methods are shown in Fig 15a and b, and it can be seen that both methods give reasonable agreement with experiment beyond $\Psi_{pol,N} \sim 0.5$. NTV is being used as one of the actuators for the rotation control algorithm being developed for NSTX-U.

Major disruptions in tokamaks can lead to halo currents that can exert large, non-axisymmetric forces resulting in localized stresses that can cause severe damage to PFCs and walls. This is unacceptable in a reactor. Most disruptions are triggered by MHD events, and a large database of NSTX disruption statistics was developed and analyzed in order to gain insight into stable operating space⁷⁵. Fig. 16 shows disruptivity as a function of β_N , q^* , pressure peaking factor $F_p = p(0)/\langle p \rangle$, shaping factor $S = q_{95} I_p / a B_T$ and l_i . Disruptivity is defined as the total number of disruptions while the plasma is in a particular operation space divided by the total time it is in that state, and $q^* \propto \frac{\varepsilon a B_T}{I_p} (1 + \kappa^2)$. While no increase in disruptivity was found for increased β_n and decreased l_i , higher disruptivity was found for low q^* , low S and high F_p and l_i .

This large database was used to develop a disruption prediction algorithm based on multi-input criteria⁷⁶. Inputs included such parameters as $n=1$ RWM amplitude, neutron emission, OH current drive power and plasma vertical motion, all evaluated in real-time. In total, 17 inputs were used to determine maximum disruption detectability while minimizing false positives (where a disruption “alarm” is declared more than 0.3 s before the actual disruption time). No single value dominated the detection algorithm; a combination of signals was required. A weighted sum of the 17 threshold tests was evaluated every 2 ms for ~ 1700 discharges, and a flag indicating an imminent disruption was set when the weighted sum was sufficiently large. Fig. 17 shows the histogram of warning times using this method. 98% of the disruptions were flagged within 10 msec, a success rate nearing the ITER requirement. Only $\sim 6\%$ were false positives. This disruption prediction algorithm will be developed further on NSTX-U.

III. Energetic Particles

The 3.5 MeV α particles produced in D-T fusion reactions will typically be super-Alfvénic, with $v_{\alpha}/v_{\text{Alfvén}} > 1$. Super-Alfvénic α particles can easily excite a variety of Alfvén modes, which in turn can modify the α population through redistribution in

energy and space, or through loss from the plasma. Not only will this impact the plasma heating by the α particles, but lost α particles can cause serious damage to plasma facing components. The neutral beam on NSTX operates with fast ion energies up to 100 keV, corresponding to approximately three to four times the Alfvén velocity, making NSTX ideal for studying these energetic particle-driven modes and mode-particle interactions. Of particular concern is how the EP modes will affect the ability to provide non-inductive current drive by the neutral beam particles, a critical component of fully non-inductive discharge scenarios.

The energetic ions from the NSTX neutral beams can destabilize a variety of toroidal Alfvén eigenmodes (TAEs), with a nominal frequency given by $\omega_{\text{TAE}} = k_{\parallel} V_{\text{Alfvén}} = V_{\text{Alfvén}} / 2qR_0$, which is in the 50 to 200 kHz range. There are TAEs that have stationary frequencies, frequencies that chirp up or down, and those whose frequencies chirp up and down simultaneously (“angel-fish”)⁷⁷. There are TAEs that are destabilized near minimum q in reversed magnetic shear discharges (rsTAE), as well those that are modified by finite β (BAEs). In addition, these effects can couple. An example of this coupling is shown in Fig. 18. Initially in this discharge, the different toroidal mode numbers appear at different times as q_{min} evolves and passes through and between low order rational surfaces. As β increases in time, these Alfvén modes start exhibiting bursting behavior, ultimately coupling among the different toroidal mode number n and resulting in TAE “avalanches”⁷⁸, which are associated with sharp, significant (>10%) drops in the measured neutron rate. Lower frequency fishbones⁷⁹ were also observed in NSTX.

Unique to STs are the presence of high frequency Compressional or Global (shear) Alfvén Eigenmodes (CAE/GAE), with characteristic frequencies in the range of 0.2 to 1.2 times the ion cyclotron frequency ($\omega_{\text{ci}} \sim 0.5$ to few MHz). As discussed in Section II, the presence of these high frequency modes is associated with a lack of electron heating at high power in the very core of NSTX plasmas, because of either enhanced electron transport due to these modes or channeling of heating power out of the core through coupling with other waves. The latter will be discussed more later in

this section. A spectrogram of various EP-induced magnetic fluctuations is shown in Fig. 19⁸⁰.

Figure 20 is an existence plot of types of Alfvén activity seen in NSTX as a function of $v_{\text{fast}}/v_{\text{Alfvén}}$ and $W_{\text{fast}}/W_{\text{total}}$. Generally, NSTX discharges evolve from the lower right of the figure to the upper left as density increases. Toroidal Alfvén Eigenmode (TAE) avalanches and other Energetic Particle Modes (EPMs) are observed at higher $W_{\text{fast}}/W_{\text{total}}$ (low and medium density), while EPMs and quiescent plasmas are seen at lower $W_{\text{fast}}/W_{\text{total}}$ (higher densities). TAE avalanches are seen when $W_{\text{fast}}/W_{\text{total}} \geq 0.3$. The figure also shows that the NSTX-U operational space (gray shaded region) in these parameters overlaps that envisioned for both ITER and an ST-FNSF. The TAE avalanches and EPMs can result in up to a 35% drop in the neutron rate, which has been determined to be due primarily from energy degradation and spatial redistribution of the fast ions. This conclusion is based on the determination of the linear eigenmode structure whose mode amplitudes are constrained by measured displacements, and particle tracking in the presence of these modes. Further, the analysis of individual TAE avalanches indicate that the energy lost from the fast ions is comparable to the estimated wave energy lost due to TAE damping on the thermal plasma.

The NOVA-K⁸¹ and ORBIT⁸² codes have been used to study the particle redistribution and neutron rate drops associated with TAE avalanches. Specifically, NOVA-K linear calculations were used to compute the ideal TAE eigenmode structure, with the amplitudes normalized to produce mode-induced radial displacements consistent with those measured by the microwave reflectometer system on NSTX. ORBIT was used to track the fast ion distribution interacting with these modes and to calculate the related neutron drop from energy and spatial redistribution, as well as actual loss from the plasma, of the fast ions. The results are shown in Fig. 21, and it is seen that there is a good match between the calculated and the measured neutron drop at the measured mode amplitude (normalized mode amplitude=1).

Recent analysis and theory have also revealed complex relationships between different instabilities. For instance, the burst frequency of high frequency Compressional Alfvén Eigenmode was found to be regulated by kink modes in the 2 to 30 kHz frequency range⁸³. The CAE burst frequency was seen to lock on the $n=1$ and 2 kink mode frequencies, with a phase shift of $\sim 90^\circ$. This repetitive bursting of modes, and coupling to kinks with this phase shift, may indicate a predator-prey relation, where the fast ion beta takes the role of the prey, increasing linearly in the absence of mode-induced losses, and the CAE mode amplitude plays the role of the predator, causing fast ion loss. Simulations with a predator-prey model find that that just a few percent modulation of the CAE damping rate is sufficient to cause the phase locking as is seen in the experiment.

In ST plasmas with weakly reversed magnetic shear and q_{\min} slightly above 1, stability calculations⁸⁴ indicate that a non-resonant kink (NRK) can be unstable. NSTX discharges have exhibited the co-existence of the NRK with higher frequency, beam-driven fishbone modes (EPMs), and linear and nonlinear simulations using the global kinetic/MHD hybrid M3D-K code⁸⁵ were carried out to study the energetic particle interaction with the NRK⁸⁶. Figure 22 shows the map of mode stability as a function of q_{\min} and $\beta_{\text{fast}}/\beta_{\text{total}}$ at fixed input power. At lower q_{\min} , the energetic ions are strongly stabilizing for the NRK (higher $\beta_{\text{fast}}/\beta_{\text{total}}$). At low fast ion population and low q_{\min} (lower left of the figure), the mode structure (inset) reflects that of a pure MHD mode with zero mode frequency and up-down symmetric structure at zero toroidal angle. At higher fast particle population and higher q_{\min} , the mode transitions to a fishbone-like energetic particle mode with a frequency comparable to the precession drift frequency. The mode structure (inset) has a twisted character. Both the NRK and the fishbone modes affect significantly the fast ion distribution, reducing the fast ion density in the central region of the plasma. The results from these linear and non-linear M3D-K calculations will be used to identify the regimes for stable operation in NSTX-U.

The excitation of high frequency Global and Compressional Alfvén modes has been

studied for an NSTX H-mode discharge using the hybrid-MHD non-linear HYM code⁸⁷. Co-rotating CAE modes were calculated to be unstable for a range of toroidal mode numbers, consistent with experimental observations⁸⁸. Results from HYM indicated that unstable CAE modes can strongly couple to kinetic Alfvén waves (KAW) on the high field side of the torus, as seen by the perturbed magnetic field structure due to the CAE and KAW modes shown in Figure 23. The resonance with the KAW is located at the edge of the CAE potential well, just inside the outer edge of the beam ion density profile. The importance of this result is that this coupling provides an energy channeling mechanism for beam energy to excite core CAE modes, with a resulting transport of energy flux away from the magnetic axis to the KAW resonance location; i.e., energy flows from the core CAE modes to the mid-radius KAW. Using the HYM-calculated linear mode structure, and estimating the magnetic perturbation level from the reflectometer displacement measurements⁸⁹, up to 0.4 MW of power can be channeled out of the core. This channeling could have a direct effect on the temperature profiles, with changes of calculated to be up to several hundred eV. This is one possible explanation for the lack of significant heating of the central T_e observed with increasing beam power and associated with CAE/GAE activity⁴⁴.

Alfvén Eigenmodes and fast ion populations can also be impacted significantly by the application of external 3D fields. Magnetic measurements of energetic ion-driven high frequency bursting CAE/GAE modes have shown that applying a $\delta B/B \sim 0.1$ to 1% $n=3$ magnetic perturbation at the plasma edge led to a reduction in mode amplitude, an increase in bursting frequency, and a smaller frequency chirp⁹⁰. The change in mode characteristics was accompanied by a drop in the neutron rate. This is due to a loss of fast ions caused directly by the change in magnetic equilibrium by the application of the 3D field. The effect of this magnetic perturbation on the fast ion distribution was calculated using the SPIRAL⁹¹ code to track the energetic particle distribution in the presence of 3D fields and a resistive plasma response calculated by the M3D-C¹ code⁹². Figure 24 shows the difference in $\partial F_{\text{fast}}/\partial v_{\perp}$ at the parallel resonant velocity with (red) and without (black) applied

magnetic perturbations, as calculated from the TRANSP and SPIRAL codes. These simulations indicate a 10 to 20% reduction in $\partial F_{\text{fast}}/\partial v_{\perp}$, the main driving term for these high frequency modes. The reduced drive is consistent with the experimentally observed reduction in mode amplitude when the 3D fields are applied.

It has also been observed that application of 3D MPs pulses could modulate TAE modes. As seen in Figure 25, 50 to 100 kHz modes were damped right after application of the MP. 3D calculations were performed using the stellarator VMEC⁹³ and STELLOPT⁹⁴ codes to determine the 3D ideal MHD equilibrium and Alfvén continuum respectively. It was found that in the presence of 3D MPs, AE gaps shrink, leading to an enhanced damping of the TAE by interaction with the continuum. These results indicate a possible path for optimizing the MPs to produce a 3D perturbed equilibrium stable against AEs.

IV. Boundary Physics

Boundary physics and power handling issues are challenging in any tokamak device, but even more so in compact STs. Very high peak divertor heat fluxes ($\geq 10 \text{ MW/m}^2$) can be reached regularly in NSTX owing to the relatively small major radius (high P/R, P/S) and the relatively short connection length between outer midplane and divertor. This is because of the steep midplane magnetic field pitch, which does not give cross-field transport as much of an opportunity for radial heat spreading. The relatively large mirror ratio and differences in turbulence at low aspect ratio are other properties that could affect the perpendicular and parallel transport in an ST. The physics of the pedestal, boundary and scrape-off layer plasmas, as well as techniques to mitigate processes causing high divertor heat flux, will be discussed in this section.

The most important and robust operational regime affecting the pedestal profiles is the H-mode, in which edge transport barriers in both density and temperature develop. H-mode discharges with lithium wall conditioning exhibited pedestal

profiles that extended to smaller minor radius than those in H-modes with boronization + HeGDC conditioning (Fig. 26). Furthermore, lithiated discharges allowed access to the “Enhanced Pedestal” (EP) H-mode regime. The transition from H-mode to EP H-mode was usually triggered by an ELM⁹⁵. Confinement enhancements in the EP H-mode were up to 50% over and above the already enhanced confinement in lithiated H-modes, and reached levels of $H_{98y,2} \sim 1.25$ to 1.7. Steady EP H-phases lasting over 0.5 s were observed⁹⁶. The EP H-mode was characterized by a region in the plasma edge with very sharp gradients in the ion temperature, typically a factor of three larger than those in the H-phase. There was also a localized region of large rotation shear in the vicinity of the steep ion temperature gradient. No changes in low-k edge turbulence going from H-modes to EP H-modes, as measured by BES, were observed.

A number of different ELM types were observed on NSTX, as is seen in Fig. 27. At low edge collisionality⁹⁷. Type I ELMs, which could result in 5 to 15% energy reductions due to each ELM, were typically observed. Just above the L-H power threshold level, Type III ELMs were observed, and they resulted in energy losses of 1 to 5%. At higher edge collisionalities, Type V ELMs occurred, but these had little or no impact on stored energy.

The pedestal stability and excitation of Type I ELMs could be described by the peeling/ballooning MHD stability model, as implemented in the ELITE code⁹⁸. In this model, the pedestal stability is determined mainly by current-driven kink-peeling modes and pressure driven ballooning modes. Fig. 28 shows the stability boundary and where the NSTX pedestal properties lie with respect to these boundaries. It is seen that the Type I ELMing discharge lies close to the peeling mode stability boundary. The pedestal width on NSTX scales as $\beta_{e,ped}$, unlike the $\beta_{e,ped}^{1/2}$ dependence observed at higher aspect ratio. This is consistent with preliminary analysis showing that KBMs can lead to different the pedestal width scalings in NSTX and other devices. The KBM paradigm on NSTX is consistent with edge turbulence measurements from Beam Emission Spectroscopy and reflectometry⁹⁹.

Linear gyrokinetic calculations using the GS2 code¹⁰⁰ were also performed to study the microstability of the plasma pedestal region¹⁰¹. Results showed that microtearing modes were unstable at the pedestal top, TEM/KBM modes unstable in the pedestal gradient region, and ETG modes unstable at the foot of the pedestal for both boronized and lithiated plasmas, irrespective of the absolute position of these locations.

Controlling ELMs is important for reducing the high transient heat loads associated with these events. Lithium application on NSTX ultimately resulted in complete suppression of ELMs, as shown in Fig. 29. Type I ELMy discharges evolved into ones with intermittent ELMs and finally into ELM-free discharges with increasing amounts of pre-shot lithium¹⁰². As the lithium application increased, the main changes at the edge were reduced density in the scrap-off layer and increased electron temperature in the pedestal region. The pedestal width increased, but the pedestal pressure gradient remained the same. This resulted in enhanced total pedestal pressure. An edge stability analysis using ELITE showed that the unlithiated plasmas that were near the kink-peeling stability boundary (Fig. 28) moved into the stable regime when lithium conditioning was used. This was because of the inward shift of the pressure and edge current peak into the reduced magnetic shear region, consistent with the disappearance of ELMs. The ELM-free discharges in NSTX often exhibited impurity and radiation buildup, which were reduced significantly by controlled ELM triggering using applied $n=3$ fields¹⁰³ or vertical jogs¹⁰⁴.

Particles and heat flow radially out of the plasma and along open field lines into the divertor region. In NSTX, peak divertor heat fluxes reached 10 MW/m^2 with 5 MW of injected neutral beam power^{105,106}. One of the plasma characteristics determining the level of heat flux is the scrape-off layer heat flux width. This width, which was inferred from IR cameras in the divertor region and mapped back to the midplane, increased with the amount of evaporated lithium, but decreased almost inversely with plasma current. The latter two effects can be seen in Fig. 30. The variation with

plasma current, or B_p , is consistent with the trend observed in a multi-device study covering a range of aspect ratio¹⁰⁷, and it is consistent in magnitude with predictions from a heuristic drift-based model assuming non-turbulent particle transport¹⁰⁸. The dependence of heat flux width on plasma current is also consistent with results from the XGC1 code¹⁰⁹, which computes the neoclassical and turbulent particle and heat transport. The heat flux widths computed by XGC-1 at two plasma currents for the 50 mg lithium deposition case are shown also in Fig. 30, and are in good agreement with experimental observations. The XGC1-calculated heat flux widths are determined primarily by neoclassical and atomic physics effects, as opposed to turbulence, for these NSTX cases.

The effect of ELMs on divertor heat flux widths has been studied in NSTX using IR-based 2D surface temperature measurements coupled to a 3D heat conduction solver¹¹⁰. The results show that under certain circumstances the heat flux footprint during large ELMs could contract by up to 50%, exacerbating the heat flux challenge. Analysis of this data indicates that the heat flux profile broadening or narrowing is directly correlated with the number of filamentary striations measured in the ELM heat flux profile; profile narrowing occurs when very few or no striations are observed in the heat flux. Figure 31 shows a measure of the change in the heat flux footprint wetted area by ELMs, relative to the value before the ELM, as a function of the number of ELM striations. The figure indicates a decrease in the wetted area and a peaking of the heat flux profile below \sim four striations. The wetted area increases almost linearly with number of striations above this value. The striations in the heat flux profile represent ELM filaments, and their number is believed to be related to the toroidal mode number of the ELMs before expulsion of the filaments. The typical range of toroidal mode numbers associated with ELM in NSTX is between one and five¹¹¹. The implications of this result for ITER and FNSF need to be assessed by determining the edge stability and most likely toroidal mode number across a range of expected temperature and density profiles. In particular, scenarios that move the projected operating points up to higher- n stability limits need to be identified in order to reduce the risk of peaking of the heat flux profiles during the ELMs.

Edge and SOL turbulence measurements have been made in order to develop an understanding of the processes controlling the radial transport of heat and particles. A deuterium gas puff imaging (GPI) diagnostic was used on NSTX to obtain detailed edge turbulence information. Camera images from the GPI show strong localized regions of light emission, called ‘blobs’, in the L-mode plasma, and a much more quiescent edge, with fewer and less intense blobs, during the H-mode (Fig. 32)¹¹². In the H-mode, blobs are seen in conjunction with ELM events. The blobs are highly elongated along field lines, i.e., are filamentary in structure, and they move both poloidally and radially. Numerical studies were carried out using the SOLT code¹¹³, which is based on a 2D curvature-interchange model. The simulations reproduce many features of the GPI measurements, including size and scale-length of the blobs, the direction of their perpendicular flow, and the inferred Reynolds acceleration (Fig. 33). The results suggest that the radial penetration of blobs is influenced by flow shear, and thus judiciously driven sheared flows in the SOL could increase the SOL heat flux width if the blobs influence this property.

The high divertor heat fluxes in NSTX generally peaked on the outer divertor, with in-out power ratios of approximately 1:4¹¹⁴. Peak heat fluxes, $q_{\text{div,peak}}$, could be reduced by operating in a double-null, rather than the usual lower single null, configuration, but the most reliable way to reduce the divertor heat flux was through divertor flux expansion, f_{exp} , which is a measure of how much the magnetic field flux from the midplane region expands to a larger surface area in the divertor region. The $q_{\text{div,peak}}$ decreased from 8 to 2 MW/m² as f_{exp} increased from 10 to 40¹¹⁵.

A technique employed on NSTX to expand the divertor flux was to operate in the “snowflake” divertor (SFD)⁵ configuration, which is based on having additional field null points close to the usual single null configuration null point, and which is related to the X-divertor concept^{116,117}. The multiple field nulls make the main X-point region larger, leading to greater flux expansion. It can be seen in Fig. 34a that the SFD configuration also offers the possibility for multiple heat channels. As seen in Fig. 34b, the SFD configuration alone resulted in a factor of three reduction in the

divertor heat flux.

Heat flux reductions of up to 60% resulted from operating the conventional divertor configuration in a partially detached regime^{118,119}. This was achieved by puffing deuterium into the divertor region to reduce the electron temperature to a few eV in front of the divertor plate, facilitating enhanced radiative cooling. This effect can also be seen in the SFD configuration, also depicted in Fig. 34b, in which the radiative cooling in the partially detached regime decreases the heat flux by an additional factor of three. Lithium coatings of ~300 mg were also found to reduce peak heat loads by up to 50%¹²⁰. The heat flux reduction was accompanied by an increase in localized radiation, as measured by bolometers near the inner and outer strike points.

As lithium wall conditioning will be the preferred technique in NSTX-U, with eventual plans to test liquid lithium modules¹²¹, studies have been conducted both in NSTX and in the laboratory to understand the characteristics of lithium surfaces exposed to plasmas and the dependence of properties of lithium coatings on the substrates on which they are deposited. Experiments in NSTX simultaneously addressed lithium sputtering from graphite tiles as well as from both heated and unheated liquid lithium divertor (LLD) modules, which had a molybdenum substrate¹²². Accumulation of carbon impurities was routinely observed in the core of ELM-free lithium-conditioned discharges in NSTX, but Li concentrations in the plasma core were less than 1% of that of carbon¹²³. There is evidence that the presence of carbon in the plasma reduces the core Li transport⁵⁵.

The temperature dependence of lithium sputtering due to impinging deuterium ions was studied both in situ and on a divertor test stand. The in situ measurements were carried out only in a limited range of LLD temperatures, from 100 to 300 C (the melting point of lithium is 180 C). Li sputtering yields in atoms/incident D⁺ for the graphite and unheated molybdenum surfaces (100 to 150 C) were similar. With heating of the LLDs, and at temperatures above the Li melting temperature (250 to 300 C), however, temperature-enhanced sputtering of the surface lithium was

observed.

In order to expand the range of lithium surface temperatures being studied, and to mimic expected NSTX-U divertor conditions, test stand studies of lithium on these metal substrates were carried out on the MAGNUM-PSI linear device at DIFFER¹²⁴. MAGNUM-PSI is a magnetized linear device designed for simulating divertor conditions expected in ITER-class devices, and it can also provide similar densities and temperatures as those found in NSTX. For NSTX-related experiments, a lithium evaporator was installed on MAGNUM-PSI, lithium was deposited onto a molybdenum substrate, and then subject to high D⁺ fluxes. Surface temperatures reached 1300 C in these experiments. While high incident D⁺ fluxes onto the target resulted in Li sputtering yields that increased with Li temperature up to 400 C and then leveled off up to 700 C, the yields were substantially lower than those measured in low incident D⁺ experiments¹²⁵. An intense cloud of lithium was observed directly in front of the target. This intense vapor cloud, which lasted for three to four seconds, resulted in a reduction of current to the target, and this offers the possibility for continuous divertor heat flux mitigation.

Surface science experiments conducted at the Princeton Plasma Physics Laboratory have been performed to understand the mechanisms for D retention in Li coatings on Mo substrates. The study shows that D is retained as LiD in metallic Li films. However, when oxygen is present in the film, either by diffusion from the subsurface at high temperature or as a contaminant during the deposition process, Li oxides are formed that retain D as LiOD. This compound liberates D₂ gas at temperatures 100 K lower than the LiD decomposition temperature. It highlights the importance of maintaining a metallic Li layer, as with flowing liquid lithium that constantly replenishes it, at increased power loading and elevated PFC temperatures in future fusion applications.

V. Solenoid-Free Operation and Wave Physics

Neutron shielding of an inboard, multi-turn OH solenoid in a fusion-energy producing compact ST design is not possible if it is to remain compact. This is because it would increase the inboard major radius of the plasma, proportionately increasing the overall device size. Thus, it is critical to develop capabilities that will allow for fully non-inductive (NI) operation in all ST discharge phases: plasma initiation, current ramp-up and sustainment. NSTX has explored co-axial helicity injection (CHI) for solenoid-free plasma initiation, and the use of RF and neutral beam-drive for NI current ramp-up and sustainment. The processes affecting the fast ion population and associated neutral beam current drive will be discussed in Sec. IV on Energetic Particles. CHI and High Harmonic Fast Wave (HHFW) physics and results will be discussed in this section.

In CHI, magnetic poloidal flux was injected into NSTX by applying a DC bias voltage, and drawing current across two electrically-isolated divertor plates⁶. A schematic of the system is shown in Fig. 35. During startup, when CHI is applied, the electrons flow in the toroidal direction since $B_T \gg B_p$, and thus current is multiplied by the number of toroidal transit times. There is a $J_p \times B_T$ force that pushes the plasma from the injection region into the main chamber, disconnecting from the electrodes through reconnection. As the poloidal field generated by the toroidal current grows, a closed flux configuration can be formed.

“Transient” CHI, was used on NSTX¹²⁶. This was developed on HIT-II and is a variant of CHI in which the injector footprints are close together and the injector current is rapidly reduced to zero. This technique resulted in ~ 160 kA of total plasma current with a multiplication factor of ~ 70 ¹²⁷. As can be seen in Fig. 36, the plasma current persisted well after the injection was turned off, reflecting a resistive current decay on closed flux surfaces. Also shown in the figure are EFIT reconstructions, indicating closed flux surfaces. Images of the plasma and closed flux formation can be seen from a sequence of visible camera images shown in Fig. 37. CHI was modeled successfully in the axisymmetric Tokamak Simulation Code (TSC)^{128,129,130}, which showed formation of closed flux surfaces as a results of generation of a strong

toroidal loop voltage that drives toroidal current. OH induction was applied to a CHI-initiated discharge, and this allowed for currents to reach 1 MA with significantly reduced ohmic flux consumption^{131,132}. CHI generated discharges that were subsequently ramped up in current using induction have also transitioned to an H-mode.

The underlying physics of CHI start-up has been studied with resistive MHD simulations using the NIMROD code¹³³ in 2D in order to improve the flux surface closure and current drive using this technique^{134,135}. A simplified model, with constant poloidal field currents and time varying injector currents, was used to study the minimum conditions for flux closure¹³⁶. In these simulations, the injector voltage was adjusted so that the $J_p \times B_T$ force overcomes the field line tension and open field lines fill the vessel. Flux closure occurred under the right conditions, i.e., approximately 0.5 ms after the injector voltage was turned off as in the experiment.

These simulations indicate that the magnetic diffusivity strongly controls flux closure, with no flux closure at high diffusivity corresponding to temperatures lower ($T_e \sim 1$ eV) than those measured in the experiment. As the diffusivity decreases with T_e increasing towards the experimental values (10 to 25 eV), flux closure occurs with increasing volume of closed flux. Field line tracing was used to confirm the formation of the X-point and flux closure, as shown in Fig. 38 for two temperatures, $T_e = 14$ and 24 eV. Additional numerical scans indicate other dependences controlling flux closure. If the injection voltage is slowly reduced to zero or the injector flux footprints are too far apart, closure is inhibited. The first is due to smaller generated toroidal loop voltage, and the second due to the longer time scales required for the oppositely directed flux to come together and form an X-point.

The simulations have shown that during X-point formation, the current density is localized to an elongated current sheet whose width scales as $\eta^{1/2}$, where η is the magnetic diffusivity. This, along with the computed strong inflow and outflow

characteristics, suggests that the X-point formation may be a Sweet-Parker¹³⁷ type reconnection.

Conventional RF heating and current drive techniques using Electron Cyclotron and Lower Hybrid waves are not practical for STs because of the wave accessibility issues in the overdense ST plasmas, where $(\omega_{pe}/\omega_{ce})^2 \gg 1$. Wave research on NSTX has therefore focused on High Harmonic Fast Waves (HHFW), which are compressional Alfvén waves but at the 10th to 20th harmonic of the ion cyclotron frequency. HHFW was predicted to damp primarily on the electrons with single pass absorption at high- β . Significant electron heating was observed in NSTX, with $T_{e0} \sim 6.2$ keV in helium and ~ 5.2 keV in deuterium at $n_{e0} \sim 1.5 \times 10^{19} \text{ m}^{-3}$, $B_T = 0.55$ T and with 3 MW of HHFW (Fig. 39)¹³⁸. The very peaked T_e profile in Fig. 39 reflects the very peaked HHFW heating profile. The precise determination of the actual HHFW heating power coupled to the main plasma could be determined from changes in the plasma stored energy when the HHFW was pulsed on and off, with heating efficiencies ranging from 40 to 80%, with the lower efficiencies at higher wave phase velocities (lower wavenumber $k_{||}$)¹³⁹. It was also found that some of the HHFW power coupled to the plasma interacted with both fast and thermal ions.

Despite the loss of heating power coupled to the core plasma, HHFW could drive significant fractions of current non-inductively through direct current drive and through enhancement of bootstrap current through electron heating. For a 300 kA discharge with HHFW, the plasma loop voltage was seen to decrease to zero, and approximately 70 to 100% of the current was calculated to be non-inductive.

The HHFW power not coupled to the plasma is lost along open field lines in the SOL, as confirmed by visible images (Fig. 40)¹⁴⁰. The power loss was found to be higher at higher density, indicating a possible relation between the power losses in the SOL and the fast wave cutoff. Understanding the physics of RF deposition and especially this loss mechanism will lead to discharge optimization where RF losses can be minimized, and can also aid in the projection of ICRF efficiency and deposition in ITER.

Full wave simulations using the AORSA code¹⁴¹ have been performed to demonstrate the direct correlation between the location of the fast wave cutoff relative to the antenna and the Last Closed Flux Surface (LCFS), the large amplitude of RF fields in the SOL, and the power loss there¹⁴². Fig. 41 shows the wave electric field obtained from AORSA for an NSTX discharge where two density values in front of the antenna, n_{ant} , were used. The white and black curves in the figure indicate the FW cutoff and LCFS respectively. It is clearly seen in the figure that the wave electric field in the SOL is small at low density, when the FW cutoff is in front of the antenna, but becomes large at high density when the FW cutoff opens up. At low density, the waves are evanescent, but they can propagate in the scrape-off layer when the cutoff opens up.

In order to understand how the variation of the electric field amplitude is associated with the wave SOL power losses, an artificial collisional damping has been incorporated into AORSA. The value of the collisional damping term was chosen so that the level of RF power loss to the SOL is consistent with that inferred from experiment¹⁴³. The actual damping mechanism is presently unknown. The fraction of RF power lost to the SOL as a function of n_{ant} rapidly increases as the wave transitions from the evanescent (low n_{ant}) to the propagating regime (high n_{ant}). This transition occurs at the density where the fast wave cutoff opens up, and at fixed B_T this density is a function of wavenumber, being lower for lower wavenumber. At fixed wavenumber, higher B_T moves the transition to higher n_{ant} (i.e., $n_{\text{ant}} \sim k_{\parallel}^2 B_T$).

Another possible mechanism causing HHFW power losses is through the parametric decay instability (PDI), which is a process where the HHFW decays into an ion Bernstein wave and an ion quasi-mode¹⁴⁴. On NSTX, such an instability was associated with strong ion heating at the plasma edge¹⁴⁵. These parasitic effects are likely to be reduced at higher toroidal field.

VI. NSTX-Upgrade

The NSTX-Upgrade, or NSTX-U¹⁸, has three overarching research goals:

1. To advance the ST concept for a Fusion Nuclear Science Facility (FNSF). Achieving this goal requires demonstrating 100% non-inductive sustainment at a performance level that extrapolates to $\geq 1 \text{ MW/m}^2$ neutron wall loading in FNSF, as well as developing non-inductive start-up and ramp-up techniques for an FNSF with small, or no, solenoid. The latter is a unique requirement for an ST-based FNSF.
2. To develop solutions for the plasma-material interface (PMI). High heat fluxes, with q_{peak} up to 40 MW/m^2 and $P_{\text{heat}}/S \sim 0.5 \text{ MW/m}^2$, which is up to five times greater than than on NSTX, will need to be mitigated.
3. To explore the unique ST parameter regimes to advance predictive capability for ITER and beyond. In order to address this goal, NSTX-U will access reduced collisionality (up to a factor of three to six lower than on NSTX), and high- β ($\beta_N \leq 6$) with an ability to vary the q and rotation profiles for enhanced stability, confinement and non-inductive current drive. Models for thermal and fast ion transport will be developed and/or tested.

A major motivation for the Upgrade is to access lower collisionality plasmas, which is important for extrapolations of confinement, stability and non-inductive current drive. As an example, Fig. 42 shows the normalized confinement time as a function of collisionality (based on Fig. 5 but with a logarithmic abscissa to make more obvious the low collisionality values relevant for an ST-based FNSF). As can be seen, the strong inverse collisionality dependence of confinement seen on NSTX extrapolates to about a factor of two higher value than for the ITER98y,2 scaling, in which the collisionality dependence is weak. NSTX-U will afford a factor of three to six reduction in collisionality in order to assess further this dependence, which could have a significant impact on the design of an ST-FNSF.

As collisionality is lowered, it is expected that the dominant turbulent modes affecting plasma transport may change. While ETG modes that can drive electron transport show little dependence on collisionality³⁴, microtearing modes may be suppressed at low collisionality, but KBM and TEM modes, both of which can cause

both electron and thermal ion transport, may become more important. As seen in the Macroscopic Stability section, RWM stability and NTV can be strongly dependent on collisionality, with RWM stability enhanced at lower collisionality with certain rotation profiles. Non-inductive current drive can also benefit from reduced collisionality through optimization of both bootstrap and neutral beam-driven currents.

In order to obtain the reduced collisionality, NSTX-U will allow for a factor of \sim two increase in plasma current and toroidal magnetic field to values of 2 MA and 1 T respectively. A major Upgrade component is a new centerstack that is slightly larger than that in NSTX, and this will result in plasmas with slightly higher aspect ratio ($R/a = 0.95/0.55 \text{ m} = 1.7$) and elongation (κ up to 2.8) than in NSTX. The centerstack will provide three to four times the ohmic flux swing as that in NSTX for inductive operation, and, coupled with predicted bootstrap and beam-driven non-inductive currents, will allow for pulse lengths up to 5 s^{146,147}. A comparison of NSTX and NSTX-U cross-sections is shown in Fig. 43.

A second major upgrade is the addition of a second neutral beam, which will have higher tangency radii than the first beam and thus inject more tangentially ($R_{\text{TAN}} = 110, 120$ and 130 cm for the three sources in the second neutral beam). Not only will this second neutral beam provide higher auxiliary heating power to access reduced collisionality, but it provides the means, through use of different combinations of the total of six beam sources, to vary and control both rotation and q profiles, both of which are important for optimizing confinement¹⁴⁸, stability⁶⁶ and non-inductive current drive^{146,18}.

Other capabilities for NSTX-U include a continuation of using transient CHI, which is projected to provide up to 400 kA of non-inductive startup current at the higher toroidal field. 400 kA is sufficient to confine fast ions from NBI for heating and current drive purposes. In the future, plasma guns, presently under development on the Pegasus ST¹⁴⁹, may be tested for non-inductive plasma initiation on NSTX-U.

Wall conditioning using boronization + HeGDC or lithium conditioning, the latter using the present two downward-pointing LITERs and eventually two additional LITERs pointing upward, will be employed. High-Z tiles will gradually be introduced into the NSTX-U divertor regions to assess the high-Z impurity transport and power handling capabilities as a possible PMI solution. High-Z PFC research will benefit both ITER operations and an ST-FNSF design. The high-Z divertor tiles would serve as substrates for novel liquid lithium divertor modules, also to be tested on NSTX-U. If the high-Z divertor tiles prove to benefit PMI solutions, there is consideration for changing all PFCs to high-Z materials.

High flux expansion snowflake or X-divertors, coupled with radiative detachment, will be employed for mitigating the high heat fluxes expected on NSTX-U. Additional PF coils in the new centerstack will enable operation with both upper and lower snowflake divertors. The multi-fluid UEDGE^{150,151} has been used to assess snowflake and impurity-seeded radiative divertors as heat flux mitigation candidates in NSTX-U. The simulations were carried out for NSTX-U plasmas with $I_p = 2$ MA, $B_T = 1$ T and 9 MW of power flow into the scrape-off layer. NSTX H-mode-level transport coefficients were assumed; $\chi_{e,i}$ was taken to be 2 m²/s at the core-edge interface ($\Psi_n = 0.9$), increasing to 4 m²/s at the separatrix and remaining constant at that value in the SOL. The perpendicular particle transport was assumed to increase from $D=0.1$ m²/s at the core-edge interface to 0.5 m²/s at the separatrix and SOL. The results of the simulation are shown in Figure 44. Both standard and snowflake divertor configurations are found to be achievable using NSTX-U divertor coils, and the top panel shows the power to the divertor in both configurations (snowflake divertor in red, standard divertor in black) as a function of density at the core-edge interface, assuming 3% carbon in the plasma. The sudden change in power to the divertor at $\sim 4 \times 10^{19}$ m⁻³ in the standard divertor configuration corresponds to the divertor detachment¹⁵². In the snowflake configuration, however, radiative, or detached operational densities extend down to $\sim 2 \times 10^{19}$ m⁻³, corresponding to $n_e/n_{GW} \sim 0.4$. The total heat fluxes are reduced by $\sim 70\%$ at moderate densities ($\sim 3.5 \times 10^{19}$ m⁻³), where the peak heat flux is reduced by 50% (middle panel). The bottom panel

shows the peak heat flux as a function of % argon for the snowflake and standard divertors. It is clear that less impurity seeding is needed in the snowflake to attain lower heat fluxes. Additional methods of heat flux mitigation being considered include strike point sweeping and lithium vapor shielding, the latter being studied on the Magnum-PSI divertor test stand¹²⁴.

Additional capabilities being considered for future upgrades include up to 1 MW of ECH, a cryopump and a set of off-midplane magnetic perturbation coils. The ECH would be used for heating start-up plasmas in order to increase coupling to HHFW and NBI for optimizing current drive¹⁴⁷. The cryopump, planned for the lower divertor region, would be used for particle and density control, critical to maintaining high performance in longer-pulse discharges. Other particle and density control methods to be tested include ELM-pacing with applied magnetic perturbations or a lithium granule injector¹⁵³. The precise design of the off-axis non-axisymmetric control coils and the resulting poloidal field spectrum is being optimized with respect to several metrics, including control of error fields and rotation, resonant magnetic perturbations for ELM control, and active resistive wall mode control.

As the ability to achieve fully non-inductive operation is one of the overarching goals of NSTX-U, simulations to develop these scenarios at 1 T have been carried out. The simulations assume non-inductive start-up currents of several hundred kA, and include HHFW, NBI and bootstrap drive mechanisms. These time-dependent simulations were carried out with the free boundary equilibrium solver ISOLVER in TRANSP, and have pointed out the importance of the availability of EC heating of CHI-initiated plasmas in order to raise the electron temperature and enhance the coupling of the start-up plasma to both HHFW and NBI. An example of such a time-dependent simulation, which was run with loop voltage constrained to zero, is shown in Fig. 45. TORAY¹⁵⁴ simulations indicate that 1 MW of EC heating can rapidly heat start-up plasmas from $T_e \sim 10$ to 20 eV, typical of CHI conditions, to about 1 keV in 30 ms. Up to 4 MW of HHFW is then used in conjunction with EC to further

heat the plasma, as calculated by TORIC¹⁵⁵, and to drive current to facilitate NBI with minimal fast ion losses. The combined EC/HHFW can delay the decrease of CHI-generated current and sustain a non-inductive current of 350 kA. With 10 MW of NBI distributed over the two beamlines, the simulation shows that the current can be ramped up non-inductively to 900 kA in 2.5 s. With the density between 60 and 90% of the Greenwald limit and $H_{98y,2} \sim 1.0$ to 1.2, the total current is sustained with a contribution from the bootstrap of between 40 and 60%. The simulation has not relaxed to a full steady-state, and this results in a finite electric field inside the plasma, which gives rise to a small, negative ohmic current.

Acknowledgements:

The author would like to express his gratitude to the NSTX Physics and Engineering Teams for their contributions to both the NSTX research program and to this manuscript. This work was supported by US Department of Energy Contract DE-AC02-09CH11466.

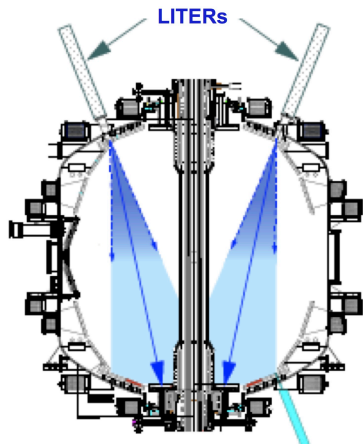


Figure 1 Schematic of LITERS and Liquid Lithium Divertor (LLD) module (left) and photo of LLD (right) on NSTX.

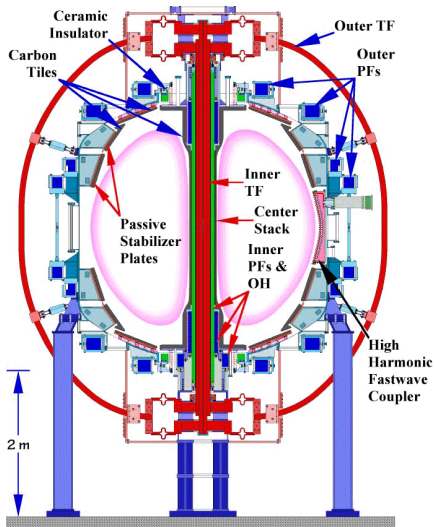


Fig. 2 (a) Schematic of NSTX device cross-section and (b) interior view

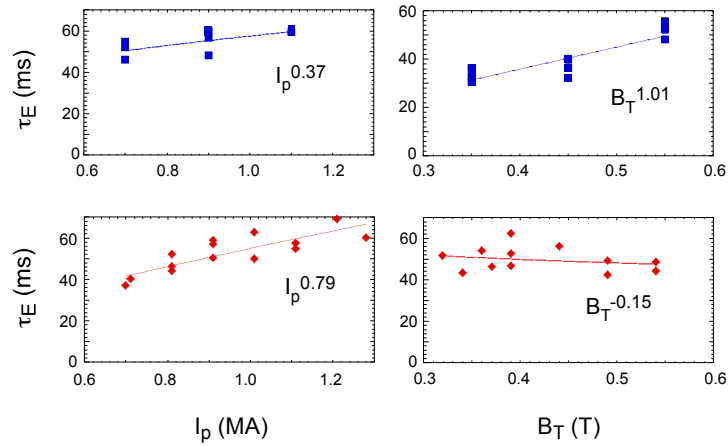


Figure 3 Thermal energy confinement scaling dependences of unlithiated (boronized) discharges (top row) and lithiated discharges (bottom row) on plasma current and toroidal field. Reproduced from Kaye et al., Nucl. Fusion **53** 063005 (2013). Copyright (2013). Institute of Physics.

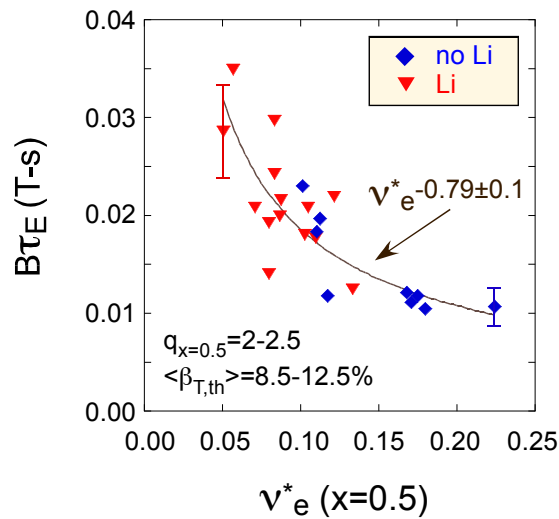


Figure 4 Dependence of normalized thermal confinement time ($\Omega \tau_E \approx B_T \tau_E$) for unlithiated and lithiated plasmas within q and β_T constraints on electron collisionality at $x = [\Phi / \Phi_a]^{1/2} = 0.5$, where Φ is the toroidal flux. Reproduced from S. Kaye et al., Nucl. Fusion **53** 063005 (2013) courtesy of IAEA.

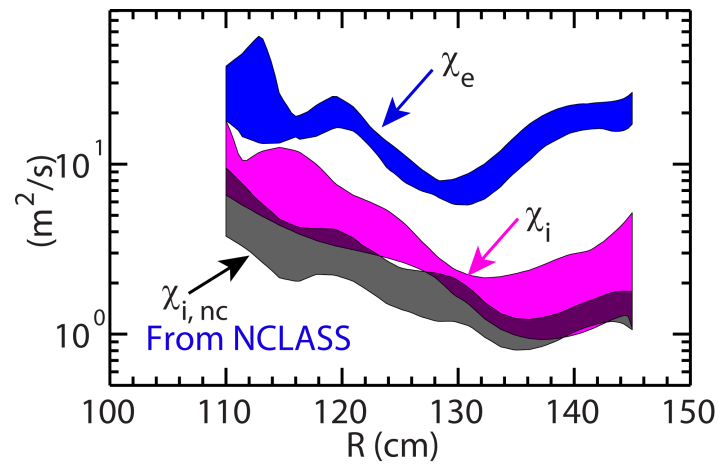


Fig. 5 Electron and ion thermal energy diffusivity profiles in NSTX H-mode Plasmas. The ion neoclassical value is also shown.

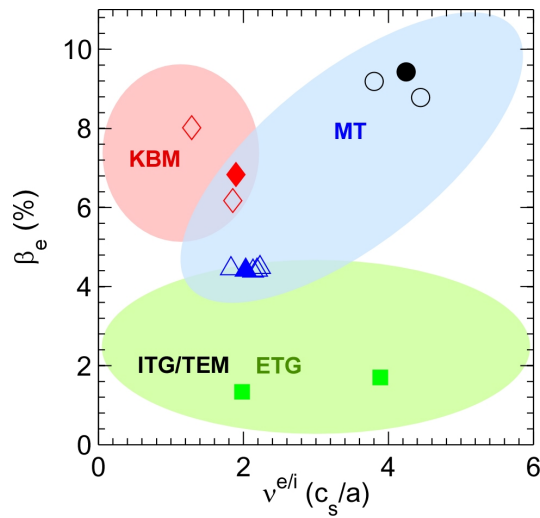


Figure 6 Local values of β_e and ν_{ei} ($r/a=0.6-0.7$) for various H-mode discharges. The colored regions illustrate where various microinstabilities are generally predicted to occur. Reproduced from W. Guttenfelder et al., Nucl. Fusion **53** 093022 (2013) courtesy of IAEA.

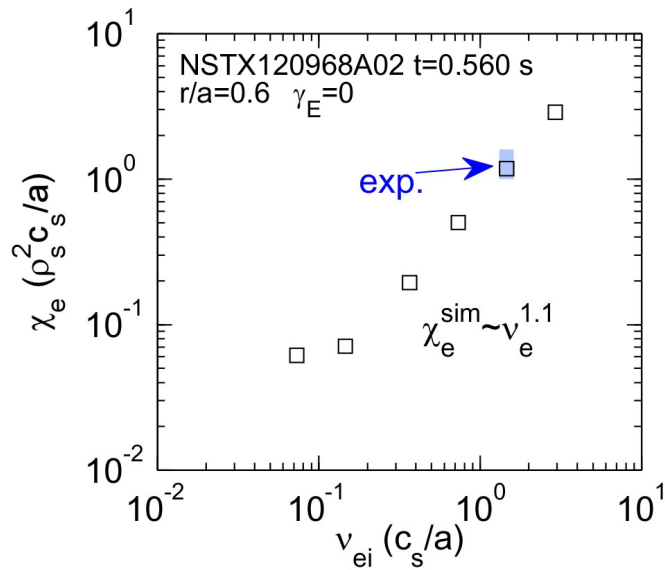


Fig. 7 Normalized electron thermal diffusivity vs normalized electron collision frequency. The shaded region shows the experimental values with uncertainties. Reproduced from W. Guttenfelder et al., Phys. Plasmas **19** 056119 (2012) American Institute of Physics.

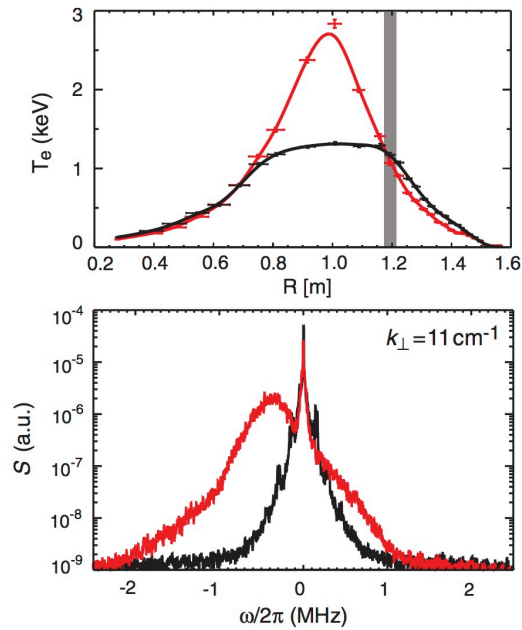


Fig. 8 Temperature profiles (top) and spectral density of fluctuations (bottom) during HRFW heating (red) and after (black). The blue stripe indicates the location of the microwave scattering measurement where L_{Te} is 15 cm and 50 cm, respectively. Negative frequencies (bottom) correspond to Doppler shifted frequency spectrum due to wave propagation in the electron diamagnetic direction. Reproduced from E. Mazzucato et al., Nucl. Fusion **49** 055001(2009) courtesy of IAEA.

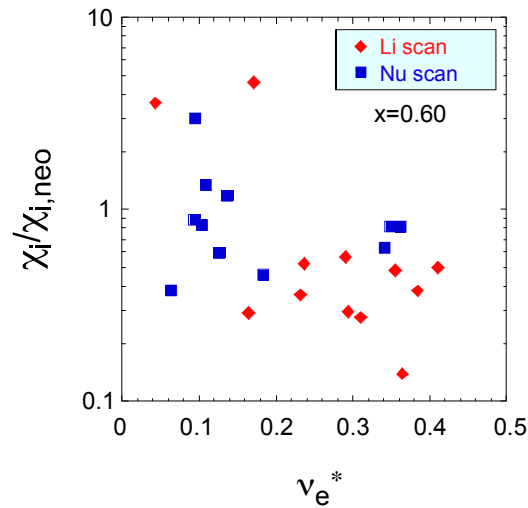


Fig. 9 Ion thermal diffusivity, χ_i , normalized to the neoclassical ion thermal Diffusivity as a function of ν_e^* at $x=0.6$. Values from lithiated (red) and unlithiated (blue) plasmas are shown. Reproduced from Kaye et al., Nucl. Fusion **53** 063005 (2013). Copyright (2013). Institute of Physics.

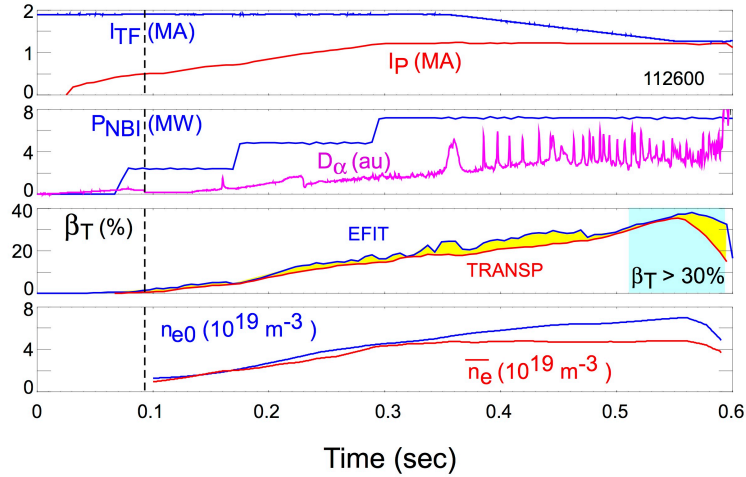


Fig. 10 Time evolution of a high- β_T discharge. Reproduced from Kaye et al., Nucl. Fusion **45** S168 (2005) courtesy of IAEA.

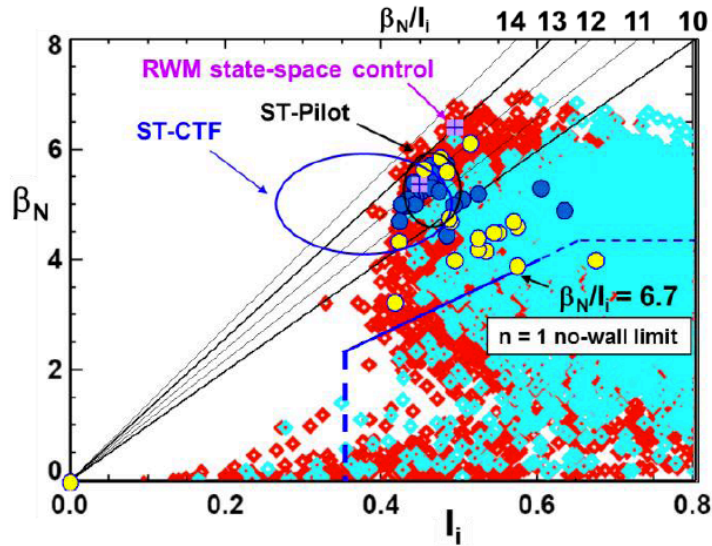


Fig. 11 High β_N , low l_i operational space in NSTX. Red/cyan points indicate plasmas with/without $n=1$ active RWM control. Blue circles indicate stable long pulse plasmas with active RWM control; yellow indicates disruptions. Reproduced from S.A. Sabbagh et al., Nucl. Fusion **53** 104007 (2013) courtesy of IAEA.

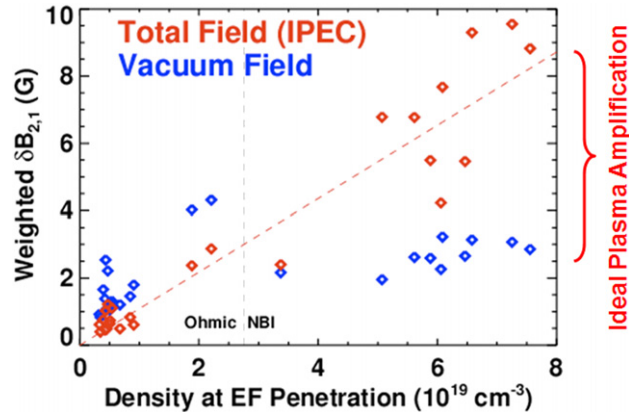


Fig. 12 Inclusion of the plasma amplification of an external error field calculated by IPEC restores a linear scaling of the threshold for mode locking with plasma density which breaks down if only the external field error is considered. Reproduced from R. Raman et al., Nucl. Fusion **51** 094011 (2011) courtesy of IAEA.

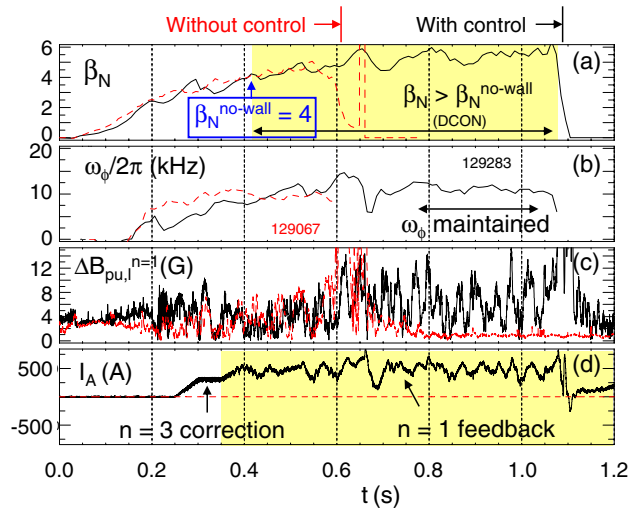


Fig. 13 High β_N discharge using $n=1$ active mode control with $n=3$ DC EF control (solid line) versus a discharge without active control (dashed line) that is terminated by an RWM instability. Frames show the evolution of (a) β_N with the shaded region indicating the period when $\beta_N > \beta_{N, \text{no wall}}$, (b) plasma rotation frequency near the $q=2$ surface, (c) $n=1$ component of the poloidal field produced by RWM activity and (d) current in one of the RWM active feedback coils. The shaded region indicates the period when $n=1$ active feedback is activated. Reproduced from S.A. Sabbagh et al., Nucl. Fusion **50** 025020 (2010) courtesy of IAEA.

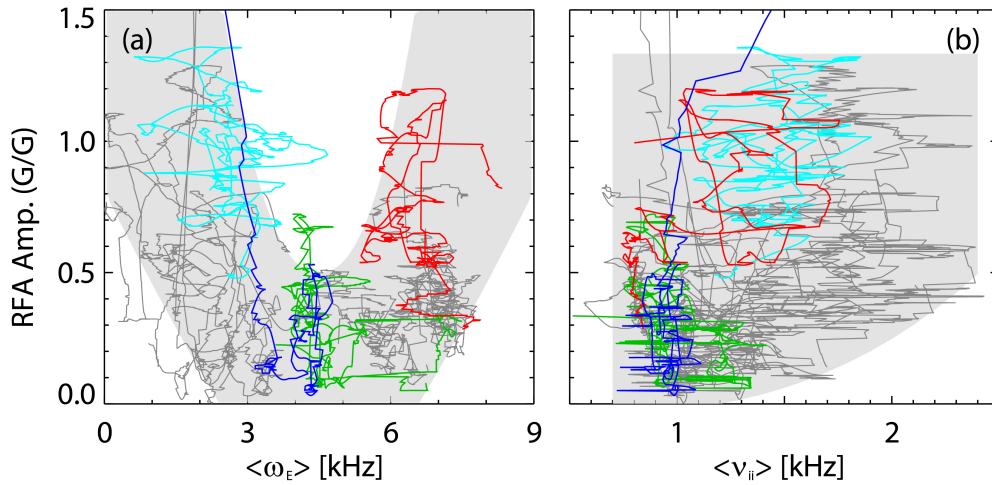


Fig. 14 (a) $n=1$ RFA amplitude as a function of ExB rotation frequency, and (b) $n=1$ RFA amplitude as a function of ion-ion collisionality, showing a relatively large change with collisionality at low RFA (“on resonance”) versus almost no change at high RFA. Reproduced from J.W. Berkery et al., Phys. Plasmas **21** 056112 (2014). Copyright (2014) American Institute of Physics.

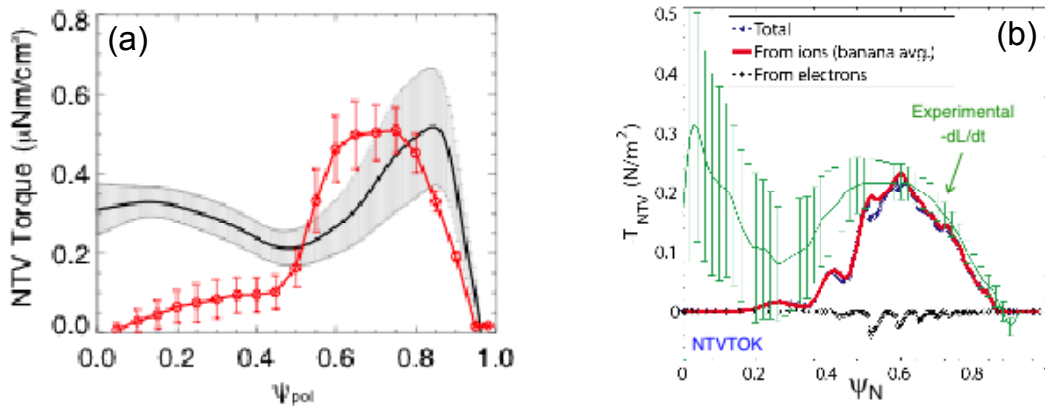


Fig. 15 (a) Experimental NTV torque density (black) and that calculated from POCA (red). Reproduced from K. Kim et al., Nucl. Fusion **54** 073014 (2014). Copyright (2014) Institute of Physics. (b) Experimental NTV torque (green) and that calculated from NTVTOK scaled by a factor of 0.6.

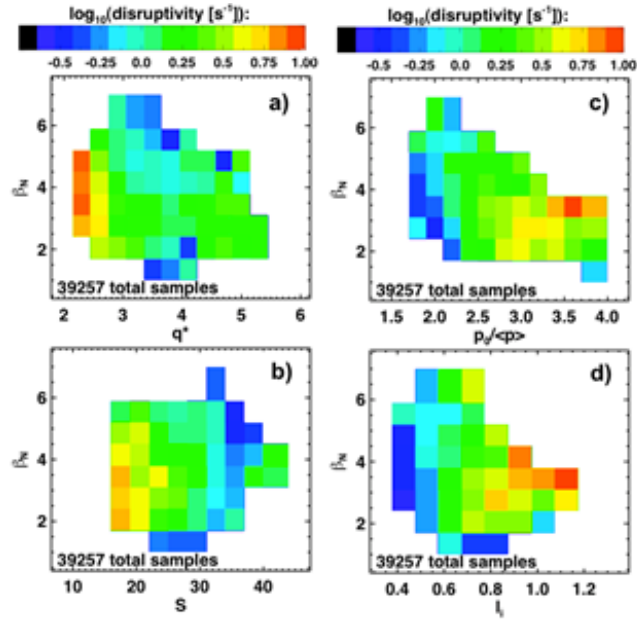


Fig. 16 Disruptivity as a function of β_N and a) q^* . b) shape factor, c) pressure peaking, and d) l_i . Reproduced from S.P. Gerhardt et al., Nucl. Fusion **53** 043020 (2013) courtesy of IAEA.

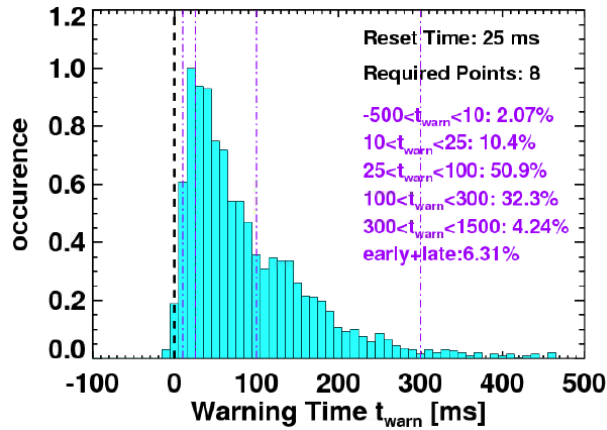


Fig. 17 Histogram of warning times computed for 1700 disruption discharges. Reproduced from S.P. Gerhardt et al., Nucl. Fusion **53** 063021 (2013) courtesy of IAEA.

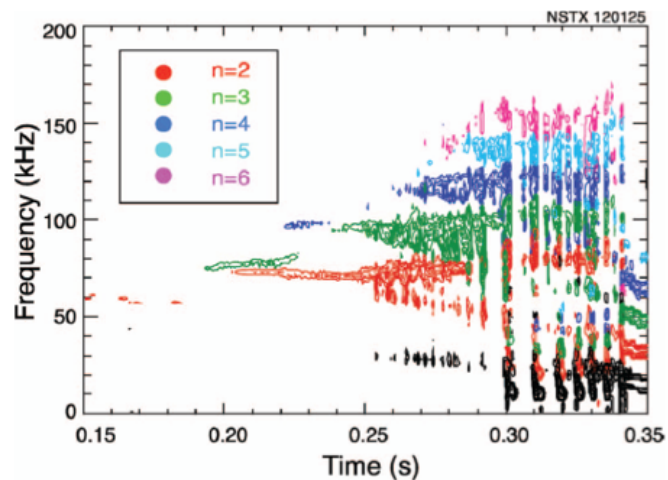


Fig. 18 Color spectrogram of Mirnov coil from discharge at the threshold beta below which Alfvén cascades are seen. Reproduced from E.D. Fredrickson et al., Phys. Plasmas **14** 102510 (2007). Copyright (2007) American Institute of Physics.

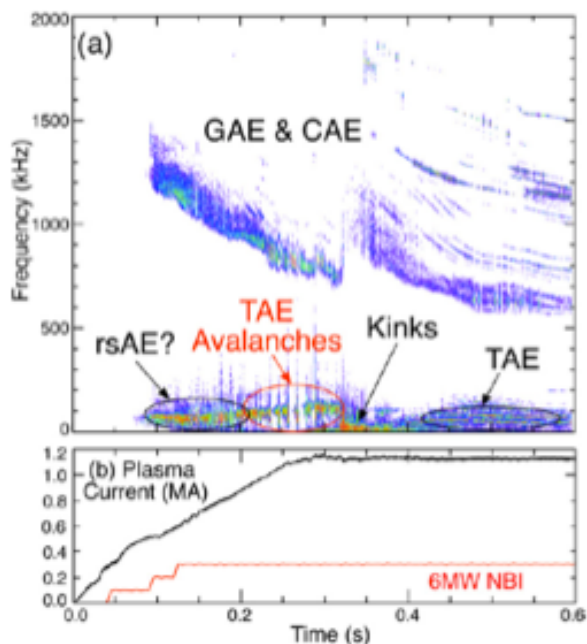


Fig. 19 (a) Spectrogram of EP induced magnetic fluctuations in NSTX, (b) plasma current and neutral beam power evolution. Reproduced from E.D. Fredrickson et al., Nucl. Fusion **53** 013006 (2013) courtesy of IAEA.

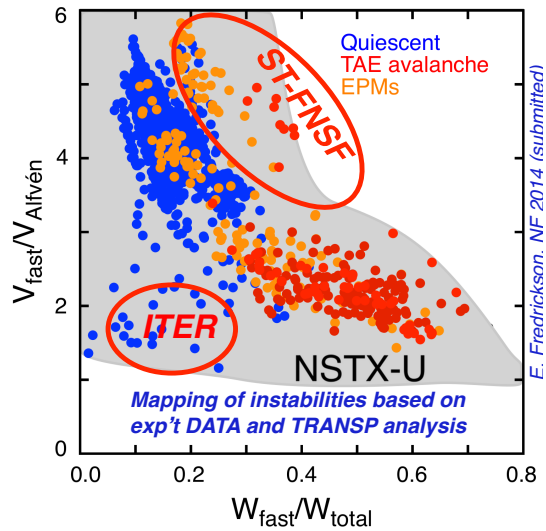


Fig. 20 Existence space for various types of Alfvén activity in NSTX. Reproduced from S.M. Kaye et al., Nucl. Fusion to be published (2015) courtesy of IAEA.

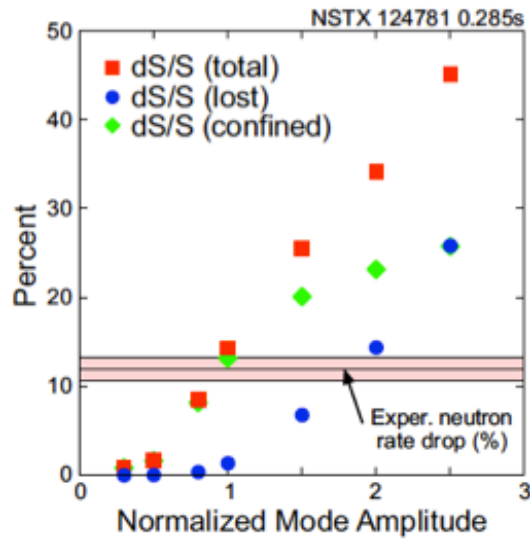


Fig. 21 Simulated neutron rate drop due to TAE avalanche (red), neutron rate drop resultsin gfrom lost beam ions (blue) and neutron rate drop from energy loss (green). Reproduced from E.D. Fredrickson et al., Nucl. Fusion 53 0130016 (2013) courtesy of IAEA.

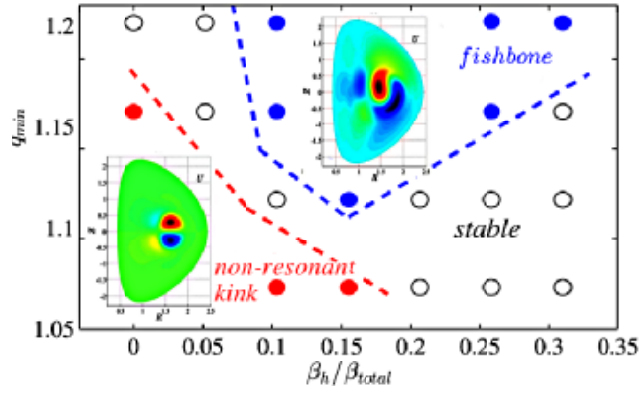


Fig. 22 Mode stability for the non-resonant kink and fishbone modes in NSTX. Insets show the linear eigenmode structure. Reproduced from F. Wang et al., Phys. Plasmas **20** 102506 (2013). Copyright (2013) American Institute of Physics.

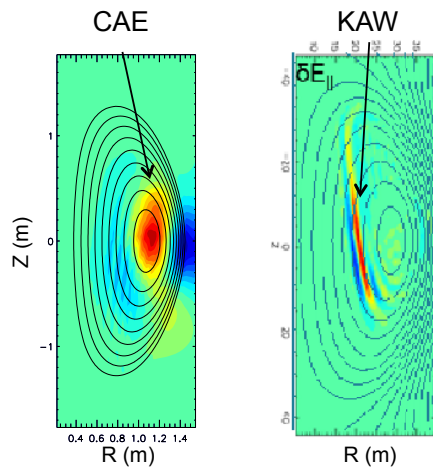


Fig. 23 Contour plots of the parallel magnetic field perturbation for CAE (left) and perturbed electric field contours for KAW (right). Reproduced from S.M. Kaye et al., Nucl. Fusion to be published (2015) courtesy of IAEA.

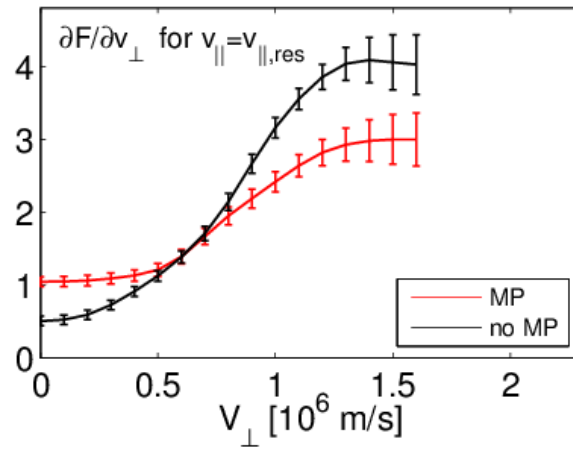


Fig. 24 $\partial F_{\text{fast}}/\partial v_{\perp}$ at the parallel resonant velocity as computed by TRANSP and SPIRAL with (red) and without (black) applied magnetic perturbations. Reproduced from S.M. Kaye et al., Nucl. Fusion to be published (2015) courtesy of IAEA.

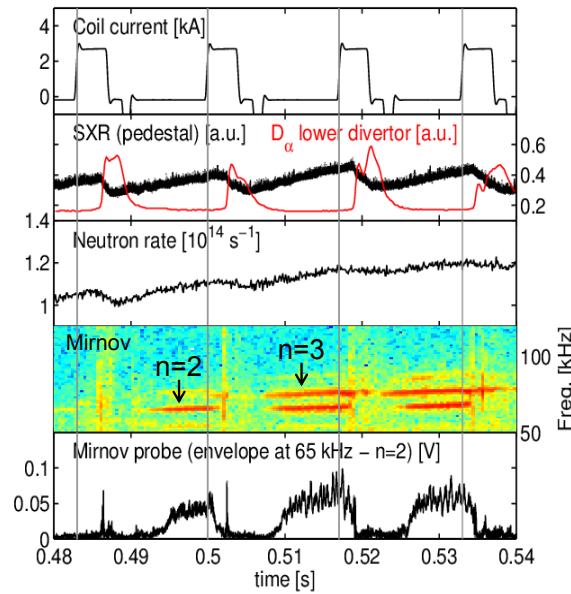


Fig. 25 TAEs modulated by pulsed edge magnetic perturbations. Reproduced from S.M. Kaye et al., Nucl. Fusion to be published (2015) courtesy of IAEA.

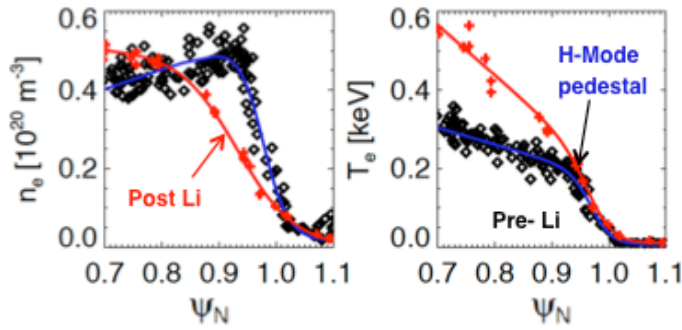


Fig. 26 Profiles for n_e and T_e for unlithiated and lithiated discharges (black and red lines respectively). Reproduced from R. Maingi. Copyright (2015) courtesy of IAEA.

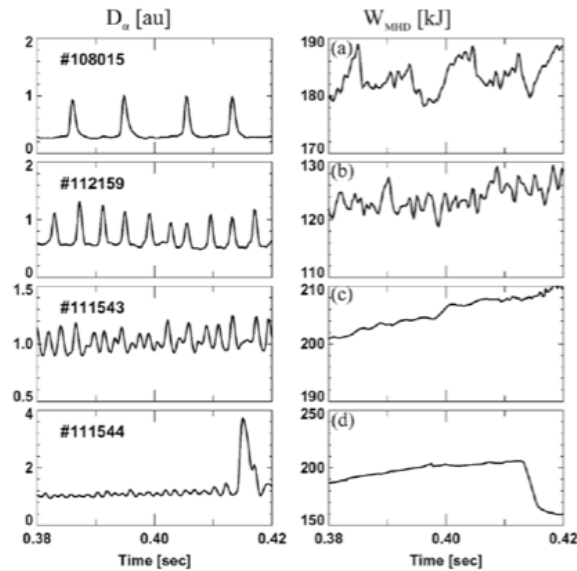


Fig. 27 Examples of different ELM types in NSTX: (a) large Type I in DN configuration (low collisionality), (b) medium Type III in configuration close to DN, (c) small Type V in LSN configuration (high collisionality) and (d) mixed Type I/Type V in LSN configuration. Reproduced from R. Maingi. Copyright (2015) courtesy of IAEA.

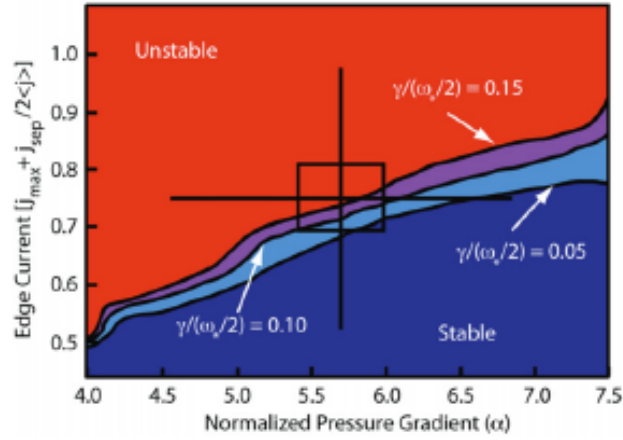


Fig. 28 Peeling-ballooning stability diagram as calculated by the ELITE code for NSTX H-mode during the Type I ELMy phase. Reproduced from A.C. Sontag et al., Nucl. Fusion 51 103022 (2011) courtesy of IAEA.

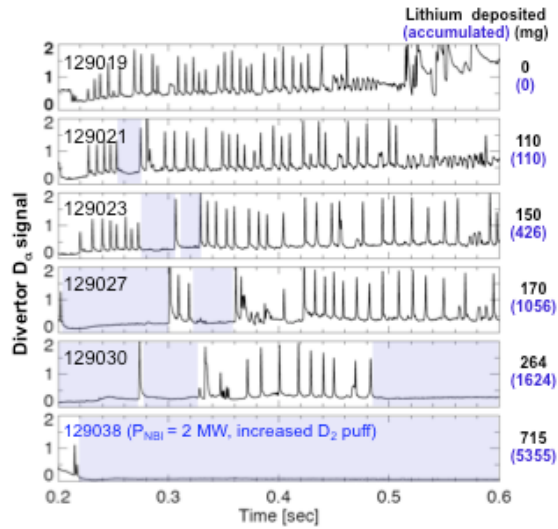


Fig. 29 Temporal edge D_a signal for various lithium deposition rates. The regularly occurring spikes represent ELMs.

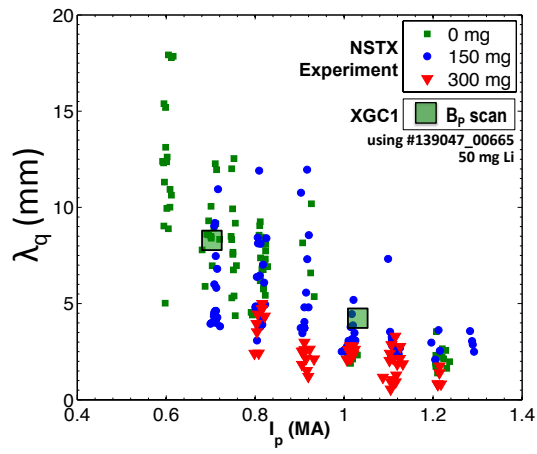


Fig. 30 Midplane scrape-off layer widths as a function of plasma current for various pre-discharge lithium deposition rates. The solid rectangles are results from the XGC1 code.

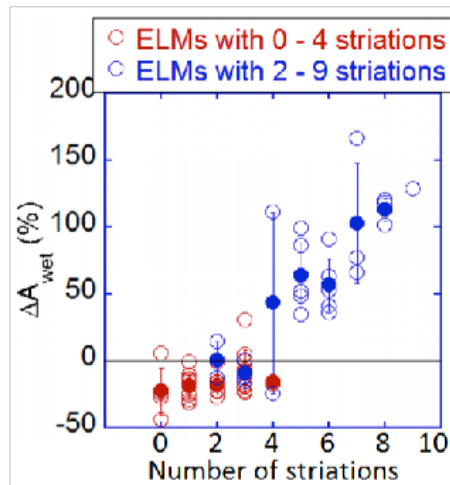


Fig. 31 Change in divertor heat flux wetted area as a function of the number of ELM striations. Reproduced from J.-W. Ahn et al., Nucl. Fusion **54** 122004 (2014) courtesy of IAEA.

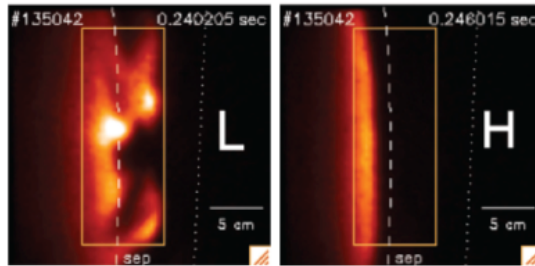


Fig. 32 Typical GPI images of the light emission in the NSTX L-mode and H-mode. Also shown in the best estimate for the separatrix location (dashed line) and the shadow of the RF antenna limiter location (dotted line). Reproduced from S.J. Zweben et al., Phys. Plasmas **17** 102502 (2010). Copyright (2010) American Institute of Physics.

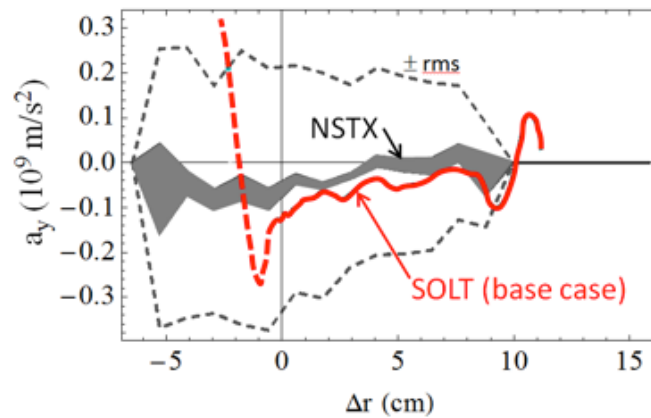


Fig. 33 Poloidal Reynolds acceleration (a_y) for seeded blob simulations (red) compared with experimental results from Gas Puff Imaging (grey). The black dashed lines represent experimental rms deviations. Reproduced from J.R. Myra et al., Nucl. Fusion **53** 073013 (2013) courtesy of IAEA.

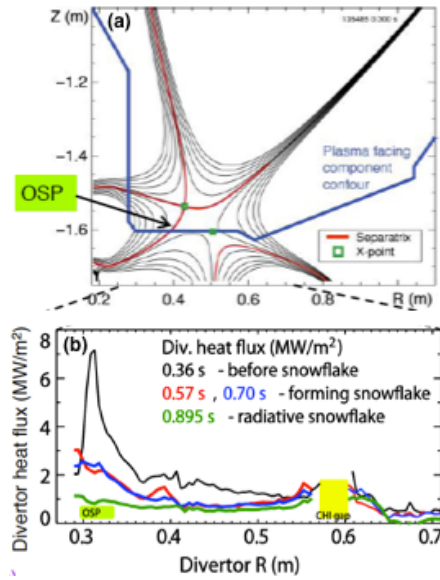


Fig. 34 (a) Poloidal flux contours for the asymmetric SFD. (b) Heat flux profile during the SFD discharge as labeled. Reproduced from V.A. Soukhanovskii et al., Phys. Plasmas **19** 082504 (2012). Copyright (2012) American Institute of Physics.

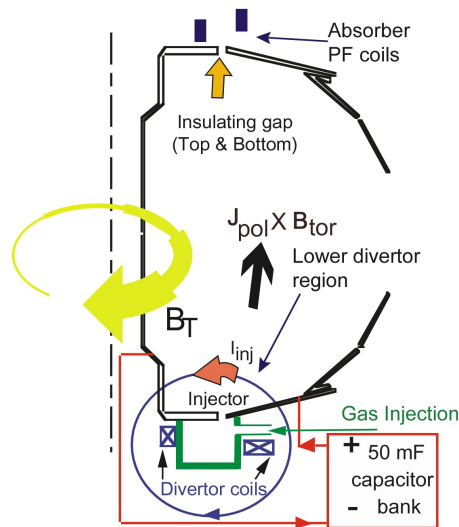


Fig. 35 Schematic drawing of the NSTX CHI system, including the location of the insulating gaps between the divertor plates. Reproduced from R. Raman et al., Phys. Rev. Lett. **97** 175002 (2006). Copyright (2006) American Physical Society.

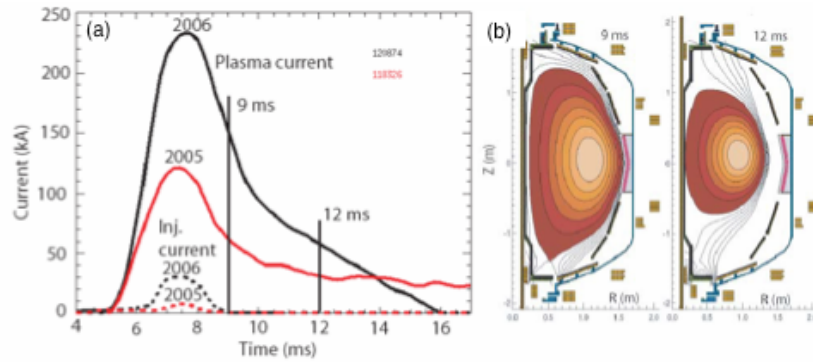


Fig. 36 (a) Discharge evolution of 160 kA closed flux current produced by CHI alone in NSTX. (b) Equilibrium reconstructions show the shape evolution of the CHI produced plasma in response to the decaying current. Reproduced from R. Raman et al., Phys. Rev. Lett. **97** 175002 (2006). Copyright (2006) American Physical Society.

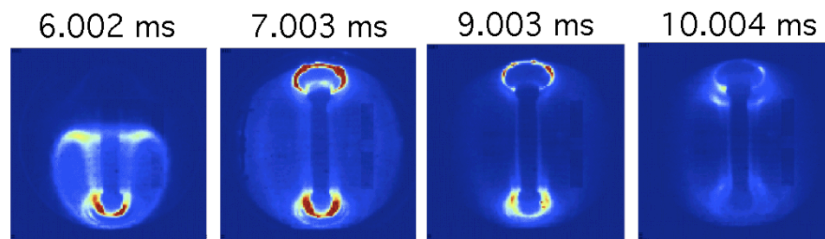


Fig. 37 Camera images of CHI plasma creation in NSTX. The injector current is zero at 9 ms when the toroidal current is 160 kA. Reproduced from D. Mueller et al., Fusion Science and Technology **52** 393 (2007).

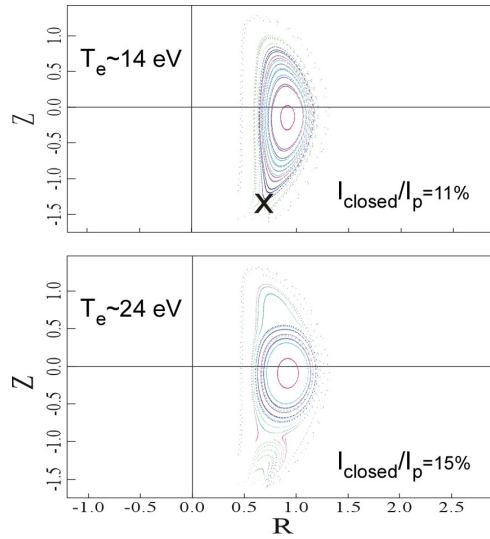


Fig. 38 Poincaré plots soon after flux closure for two experimentally-relevant electron temperatures (top) 14 eV and (bottom) 24 eV. Reproduced from F. Ebrahimi et al., Plasma Phys. **20** 090702 Copyright 2013, American Institute of Physics.

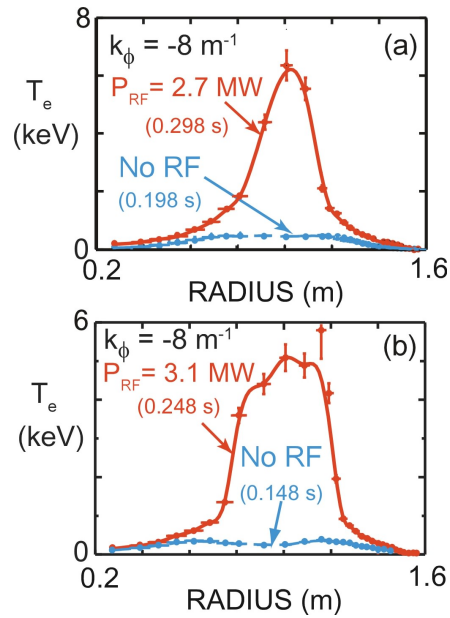


Fig. 39 (a) $T_e(R)$ immediately prior to HHFW heating (dashed blue line) and during 2.7 MW of $k_r = -8 \text{ m}^{-1}$ heating (solid line) of a helium plasma. (b) same for 3.1 MW of HHFW heating in a deuterium plasma. Reproduced from G. Taylor et al., Phys. Plasmas **17** 056114 (2010). Copyright (2010) American Institute of Physics.

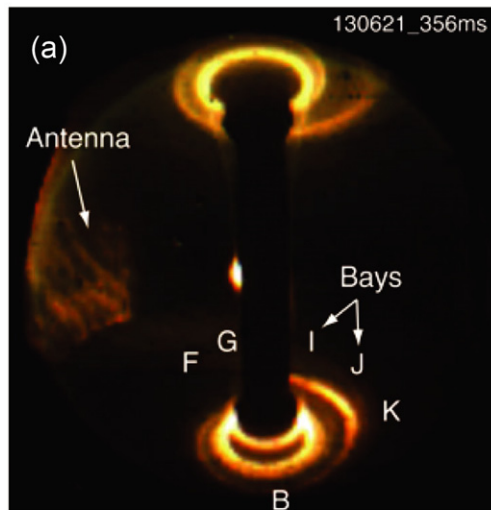


Fig. 40 Visible camera image of HRFW power interaction with the edge plasma and resulting heat spirals on the upper and lower divertors. Reproduced from R. Perkins et al., Phys. Rev. Lett. **109** 045001 (2012). Copyright (2012) American Physical Society.

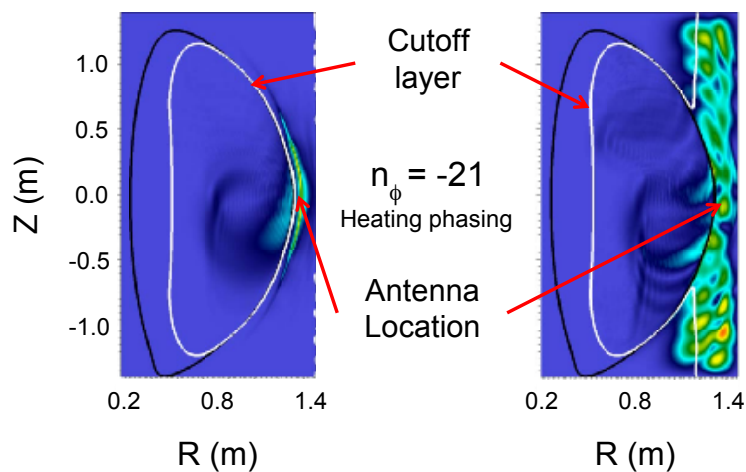


Fig. 41 Wave electric field from AORSA for low density $n_{\text{SOL}}=1 \times 10^{18} \text{ m}^{-3}$ (left) and high density $n_{\text{SOL}}=2 \times 10^{18} \text{ m}^{-3}$ (right) at the front of the antenna. Adapted from N. Bertelli et al., Nucl. Fusion **54** 083004 (2014) courtesy of IAEA.

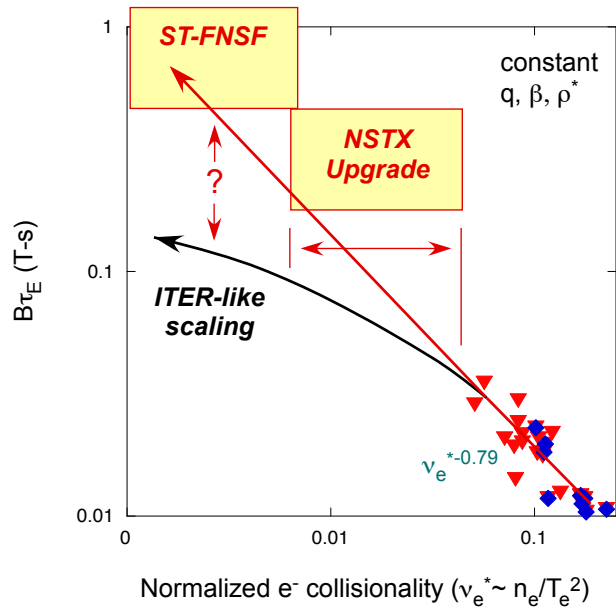


Fig. 42 Normalized confinement time as a function of normalized collisionality. Data shown are from NSTX.

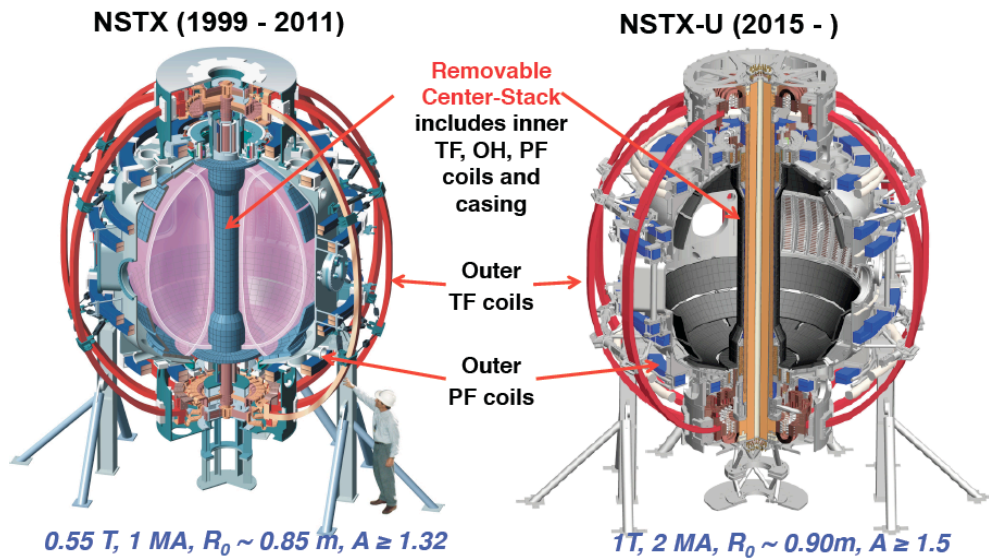


Fig. 43 Comparison of NSTX (left) and NSTX-U cross-sections.

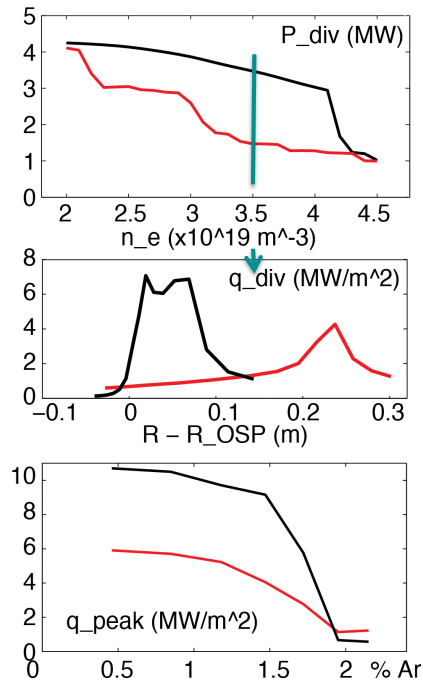


Fig. 44 (Top panel) Total heat flux to the divertor in the snowflake (red) and standard (black) divertor configurations as a function of density at the core-edge interface ($Y_n=0.9$). (Middle panel) Heat flux profiles at $3.5 \times 10^{19} \text{ m}^{-3}$ as a function of R_{OSP} , where R_{OSP} is the outer strike point radius. (Bottom panel) Heat flux to the divertor target as a function of % argon impurity seeding at $3.5 \times 10^{19} \text{ m}^{-3}$.

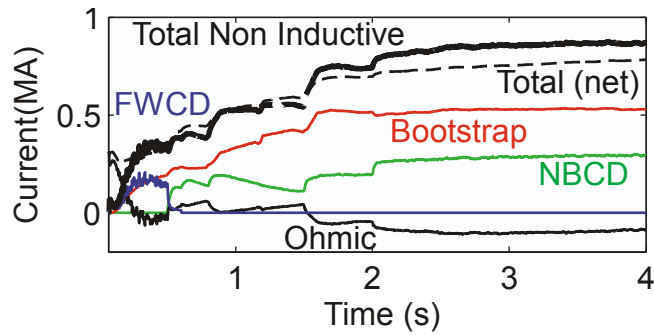


Fig. 45 Fully non-inductive current scenario for a 1 T NSTX-U discharge as computed by TRANSP with the ISOLVER free boundary equilibrium solver.

-
- ¹ Wilson, H.R. et al., Nucl. Fusion **44** 917 (2004)
 - ² Menard, J.E. et al., Nucl. Fusion **51** 103014 (2011)
 - ³ Kaye, S.M. et al., Fusion Tech. **36** 16 (1999)
 - ⁴ Ono, M. et al., Nucl. Fusion **41** 1435 (2001)
 - ⁵ Ryutov, D. et al., Phys. Plasmas **14** 064502 (2007)
 - ⁶ Jarboe, T.R., Fusion Tech. **15** 7 (1989)
 - ⁷ Raman, R. et al., Phys. Rev. Lett. **97** 175002 (2006)
 - ⁸ Kugel, H.W. et al., Phys. Plasmas **15** 056118 (2008)
 - ⁹ Kugel, H.W. et al., Fus. Eng. Design **87** 1724 (2012)
 - ¹⁰ Synakowski, E.J. et al., Nucl. Fusion **43** 1653 (2003)
 - ¹¹ Kaye, S.M. et al., Nucl. Fusion **45** S168 (2005)
 - ¹² Menard, J.E. et al., Nucl. Fusion **47** S645 (2007)
 - ¹³ Gates, D.A. et al., Nucl. Fusion **49** 104016 (2009)
 - ¹⁴ Raman, R. et al., Nucl. Fusion **51** 094011 (2011)
 - ¹⁵ Sabbagh, S.A. et al., Nucl. Fusion **53** 104007 (2013)
 - ¹⁶ Kaye, S.M. et al., accepted for publication in Nucl. Fusion (2015)
 - ¹⁷ Ono, M. and R. Kaita, Phys. Plasmas **22** 040501 (2015)
 - ¹⁸ Menard, J.E. et al., Nucl. Fusion **52** 083015 (2012)
 - ¹⁹ Rewoldt, G. et al., Phys. Plasmas **3** 1667 (1996)
 - ²⁰ Maingi, R et al., Nucl. Fusion **50** 064010 (2010)
 - ²¹ Kaye, S.M. et al., Nucl. Fusion **51** 113019 (2011)
 - ²² Bush, C.E. et al., Phys. Plasmas **10** 1755 (2003)
 - ²³ Chang, C.S. et al., Phys. Plasmas **11** 2649 (2004)
 - ²⁴ Battaglia, D. et al., Nucl. Fusion **53** 113032 (2013)
 - ²⁵ Kaye, S.M. et al., Nucl. Fusion **46** 848 (2006)
 - ²⁶ Kaye, S.M. et al., Phys. Rev. Lett. **98** 175002 (2007)
 - ²⁷ Kaye, S.M. et al., Nucl. Fusion **47** 499 (2007)
 - ²⁸ ITER Physics Basis, Nucl. Fusion **39** 2137 (1999)
 - ²⁹ Kaye, S.M. et al., Nucl. Fusion **53** 063005 (2013)
 - ³⁰ Wong, K.L. et al., Phys. Plasmas **15** 056108 (2008)
 - ³¹ Guttenfelder, W.G. et al., Phys. Plasmas **19** 022506 (2012)
 - ³² Candy, J. and R. Waltz, J. Comput. Phys. **186** 545 (2003)
 - ³³ Guttenfelder, W.G. et al., Phys. Plasmas **19** 056119 (2012)
 - ³⁴ Guttenfelder, W.G. et al., Nucl. Fusion **53** 093022 (2013)
 - ³⁵ Kaye, S.M. et al., Phys. Plasmas **21** 082510 (2014)
 - ³⁶ Jenko, F. et al., Phys. Plasmas **8** 4096 (2001)
 - ³⁷ Mazzucato, E. et al., Nucl. Fusion **49** 055001 (2009)
 - ³⁸ Wang, W. et al., Phys. Plasmas **17** 075211 (2010)
 - ³⁹ Ethier, S. et al., IAEA Fusion Energy Conference, Paper TH/P4-08 (2010)
 - ⁴⁰ Peterson, J.L. et al., Phys. Plasmas **19** 056120 (2012)
 - ⁴¹ Yuh, H. et al., Phys. Plasmas **16** 056120 (2009)
 - ⁴² Yuh, H. et al., Phys. Rev. Lett. **106** 055003 (2011)
 - ⁴³ Ren, Y. et al., Phys. Rev. Lett. **106** 165005 (2011)
 - ⁴⁴ Stutman, D. et al., Phys. Rev. Lett. **102** 115002 (2009)

-
- 45 Gorelenkov, N.N. et al., Nucl. Fusion **50** 084012 (2010)
- 46 Belova, E. et al., submitted to Phys. Rev. Lett. (2015)
- 47 Kaye, S.M. et al., Nucl. Fusion **49** 045010 (2009)
- 48 Solomon, W. et al., Phys. Rev. Lett. **101** 065004 (2008)
- 49 Hahm, T.S. et al., Phys. Plasmas **14** 072302 (2007)
- 50 Peeters, A. et al., Phys. Rev. Lett. **98** 265003 (2007)
- 51 Hulse, R.A., Nucl. Technol. Fusion **3** 259 (1983)
- 52 Behringer, K., Rep. JET-R(87)08, JET Joint Undertaking (1987)
- 53 Delgado-Aparicio, L. et al., Nucl. Fusion **49** 085028 (2009)
- 54 Clayton, D. et al., Plasma Phys. Cont. Fusion **54** 105022 (2012)
- 55 Scotti, F. et al., Nucl. Fusion **53** 083001 (2013)
- 56 Lao, L.L. et al. Nucl. Fusion **25** 1611 (1985)
- 57 Sabbagh, S.A. et al., Nucl. Fusion **41** 1601 (2001)
- 58 Hawryluk, R.J., *An empirical approach to tokamak transport* in Physics of Plasmas Close to Thermonuclear Conditions, Proceedings Course (Varenna 1979) vol. 1 p. 19 (1980)
- 59 Goldston, R.J., J. Comput. Phys. **43** 61 (1981)
- 60 Park, J.-K. et al., Phys. Plasmas **14** 052110 (2011)
- 61 La Haye, R.J. et al., Phys. Plasmas **19** 062506 (2012)
- 62 Sabbagh, S.A. et al., Nucl. Fusion **44** 560 (2004)
- 63 Sabbagh, S.A. et al., Nucl. Fusion **46** 635 (2006)
- 64 Bondeson, A. and M.S. Chu, Phys. Plasmas **3** 3013 (1996)
- 65 Berkery, J.W. et al., Phys. Rev. Lett. **104** 035003 (2010)
- 66 Berkery, J.W. et al., Phys. Plasmas **17** 082504 (2010)
- 67 Berkery, J.W. et al., Phys. Plasmas **21** 056112 (2014)
- 68 Hu, B. and R. Betti, Phys. Rev. Lett. **93** 105002 (2004)
- 69 Berkery, J.W. et al., Phys. Rev. Lett. **106** 075004 (2011)
- 70 Menard, J.E. et al., Phys. Rev. Lett. **113** 255002 (2014)
- 71 Zhu, W. et al., Phys. Rev. Lett. **96** 225002 (2006)
- 72 Kim, K. et al., Nucl. Fusion **54** 073014 (2014)
- 73 Shaing, K.C. and J. Callen, Phys. Fluids **26** 3315 (1983)
- 74 Sun, Y. et al., Nucl. Fusion **51** 053015 (2011)
- 75 Gerhardt, S.P. et al., Nucl. Fusion **53** 043020 (2013)
- 76 Gerhardt, S.P. et al., Nucl. Fusion **53** 063021 (2013)
- 77 Fredrickson, E.D. et al., Phys. Plasmas **13** 056109 (2006)
- 78 Fredrickson, E.D. et al., Phys. Plasmas **14** 102510 (2007)
- 79 McGuire, K. et al., Phys. Rev. Lett. **50** 891 (1983)
- 80 Fredrickson, E.D. et al., Nucl. Fusion **53** 013006 (2013)
- 81 Cheng, C.Z., Phys. Rep. **211** 1-51 (1992)
- 82 White, R.B. and M.S. Chance, Phys. Fluids **27** 2455 (1984)
- 83 Fredrickson, E.D. et al., Phys. Plasmas **20** 042112 (2013)
- 84 Wang, F. et al., Phys. Plasmas **20** 072506 (2013)
- 85 Park, W. et al., Phys. Plasmas **6** 1796 (1999)
- 86 Wang, F. et al., Phys. Plasmas **20** 102506 (2013)
- 87 Belova, E. et al., Phys. Plasmas **10** 3240 (2002)

-
- ⁸⁸ Fredrickson, E.D. et al., Phys. Rev. Lett. **87** 145001 (2001)
⁸⁹ Crocker, N.A. et al., Nucl. Fusion **53** 043017 (2013)
⁹⁰ Bortolon, A. et al., Phys. Rev. Lett. **110** 265008 (2013)
⁹¹ Kramer, G. et al., Plasma Phys. Cont. Fusion **55** 025053 (2013)
⁹² Ferraro, N. et al., J. Comp. Phys. **228** 7742 (2009)
⁹³ Hirshman, S.P. and J.C. Whitson, Phys. Fluids **26** 3553 (1983)
⁹⁴ Spong, D.A. et al., Nucl. Fusion **41** 711 (2001)
⁹⁵ Maingi, R. et al., Phys. Rev. Lett. **105** 135004 (2010)
⁹⁶ Gerhardt, S.P. et al., Nucl. Fusion **54** 083021 (2014)
⁹⁷ Maingi, R. et al., J. Nucl. Mater. **337-339** 727 (2005)
⁹⁸ Snyder, P.B. et al., Phys. Plasmas **9** 2037 (2002)
⁹⁹ Diallo, A. et al., Nucl. Fusion **53** 093026 (2013)
¹⁰⁰ Kotschenreuther, M. et al., Comp. Phys. Comm. **88** 128 (1995)
¹⁰¹ Canik, J.M. et al., Nucl. Fusion **53** 113016 (2013)
¹⁰² Maingi, R. et al., Phys. Rev. Lett. **103** 075001 (2009)
¹⁰³ Canik, J.M. et al., Phys. Rev. Lett. **104** 045001 (2010)
¹⁰⁴ Gerhardt, S.P. et al., Nucl. Fusion **50** 064015 (2010)
¹⁰⁵ Gates, D.A. et al., Phys. Plasmas **13** 056122 (2006)
¹⁰⁶ Soukhanovskii, V.A. et al., Phys. Plasmas **19** 082504 (2012)
¹⁰⁷ Eich, T. et al., Nucl. Fusion **53** 093031 (2013)
¹⁰⁸ Goldston, R.J., Nucl. Fusion **52** 013009 (2012)
¹⁰⁹ Ku, S. et al., Nucl. Fusion **49** 115021 (2009)
¹¹⁰ Ahn, J.-W. et al., Nucl. Fusion **54** 122004 (2014)
¹¹¹ Boyle, D.P. et al., Plasma Phys. Cont. Fusion **53** 105011 (2011)
¹¹² Zweben, S.J. et al., Phys. Plasmas **17** 102502 (2010)
¹¹³ Myra, J.R. et al., Nucl. Fusion **53** 073013 (2013)
¹¹⁴ Soukhanovskii, V.A. et al., J. Nucl. Mater. **337** 475 (2005)
¹¹⁵ Gray, T.K. et al., J. Nucl. Mater. **415** S360 (2011)
¹¹⁶ Takase, H., J. Phys. Soc. Japan **70** 609 (2001)
¹¹⁷ Kotschenreuther, M. et al., Phys. Plasmas **14** 072502 (2007)
¹¹⁸ Soukhanovskii, V.A. et al., Phys. Plasmas **16** 022501 (2009)
¹¹⁹ Soukhanovskii, V.A. et al., Nucl. Fusion **49** 095025 (2009)
¹²⁰ Gray, T.K. et al., Nucl. Fusion **54** 023001 (2014)
¹²¹ Jaworski, M.A. et al, Plasma Phys. Cont. Fusion **55** 124040 (2013)
¹²² Kugel, H.W. et al., Fusion Eng. Design **85** 865 (2010)
¹²³ Podesta, M.A. et al., Nucl. Fusion **52** 037001 (2012)
¹²⁴ DeTemmerman, C.G. et al., Journ. Vac. Sci. Technol. **A30** 041306 (2012)
¹²⁵ Abrams, T. et al., J. Nucl. Mat., in press (2015)
¹²⁶ Raman R. et al., Phys. Rev. Lett. **90** 075005 (2003)
¹²⁷ Raman R. et al, Phys. Rev. Lett. **7** 175002 (2006)
¹²⁸ Raman R. et al., Nucl. Fusion **51** 113018 (2011)
¹²⁹ Jardin, S.C. et al., J. Comput. Phys. **66** 481 (1986)
¹³⁰ Jardin, S.C. et al., Nucl. Fusion **33** 371 (1993)
¹³¹ Nelson, B.A., et al., Nucl. Fusion **51** 063008 (2011)
¹³² Raman, R., et al., Nucl. Fusion **53** (2013) 073017

-
- 133 Sovinec, C.R. et al., J. Comput. Phys. **195** 355 (2004)
134 Hooper, E.B. et al., Phys. Plasmas **20** 092510 (2013)
135 Ebrahimi, F. et al., Phys. Plasmas **20** 090702 (2013)
136 Ebrahimi, F. et al., Phys. Plasmas **21** 056109 (2014)
137 Parker, E.N., J. Geophys. Res. **62** 509 (1957)
138 Taylor, G. et al., Phys. Plasmas **17** 056114 (2010)
139 Hosea, J. et al., Phys. Plasmas **15** 056104 (2008)
140 Perkins, R.J. et al., Phys. Rev. Lett. **109** 045001 (2012)
141 Jaeger, R.F. et al., Phys. Plasmas **8** 1573 (2001)
142 Bertelli, N. et al., Nucl. Fusion **54** 083004 (2014)
143 Perkins, R.J. et al., Nucl. Fusion **53** 083025 (2013)
144 Skiff, F. et al., Phys. Fluids **27** 1051 (1984)
145 Biewer, T. et al., Phys. Plasmas **12** 056108 (2005)
146 Gerhardt, S.P. et al., Nucl. Fusion **52** 083020 (2012)
147 Poli, F.M. et al., accepted for publication in Nucl. Fusion (2015)
148 Ding, S. et al., Plasma Phys. Cont. Fusion **52** 015001 (2010)
149 Gartska, G.D. et al., Phys. Plasmas **10** 1705 (2003)
150 Rognlien, T.D. et al., J. Nucl. Mater. **196** 347 (1992)
151 Rognlien, T.D. et al., Fus. Eng. Design **60** 497 (2002)
152 Meier, E.T. et al., Nucl. Fusion **55** 086002(2015)
153 Mansfield, D. et al., Nucl. Fusion **53** 113023 (2013)
154 Lin Liu, Y.R. et al., Phys. Plasmas **10** 4064 (2003)
155 Brambilla, M., Plasma Phys. Cont. Fusion **41** 1 (1999)

Princeton Plasma Physics Laboratory Office of Reports and Publications

Managed by
Princeton University

under contract with the
U.S. Department of Energy
(DE-AC02-09CH11466)

P.O. Box 451, Princeton, NJ 08543
Phone: 609-243-2245
Fax: 609-243-2751

E-mail: publications@pppl.gov

Website: <http://www.pppl.gov>